

1 **Thermal-Driven Graupel Generation Process to Explain Dry-**  
2 **Season Convective Vigor over the Amazon**

3  
4 **Authors:** Toshi Matsui<sup>1&2</sup>, Daniel Hernandez-Deckers<sup>3</sup>, Scott E. Giangrande<sup>4</sup>, Thiago S. Biscaro<sup>5</sup>,  
5 Ann Fridlind<sup>6</sup>, and Scott Braun<sup>1</sup>

6  
7 <sup>1</sup> *Mesoscale Atmospheric Processes Laboratory, NASA Goddard Space Flight Center, Greenbelt,*  
8 *MD, USA*

9 <sup>2</sup> *Earth System Science Interdisciplinary Center – ESSIC, University of Maryland, College Park,*  
10 *MD, USA*

11 <sup>3</sup> *Grupo de Investigación en Ciencias Atmosféricas, Departamento de Geociencias, Universidad*  
12 *Nacional de Colombia, Bogotá, Colombia*

13 <sup>4</sup> *Environmental and Climate Sciences Department, Brookhaven National Laboratory, Upton, NY,*  
14 *USA*

15 <sup>5</sup> *Meteorological Satellites and Sensors Division, National Institute for Space Research,*  
16 *Cachoeira Paulista, São Paulo, Brazil*

17 <sup>6</sup> *NASA Goddard Institute for Space Studies, New York, NY, USA*

18

19 Submitted to EGU Atmospheric Chemistry and Physics (ACP)

20

21

22 **Correspondence to:** Toshi Matsui, [Toshihisa.Matsui-1@nasa.gov](mailto:Toshihisa.Matsui-1@nasa.gov)

23 **Abstract.** Large-eddy simulations (LESs) are conducted for each day of the intensive observation  
24 periods (IOPs) of the Green Ocean Amazon (GoAmazon) field campaign to characterize the  
25 updrafts and microphysics within deep convective cores while contrasting those properties  
26 between Amazon wet and dry seasons. Mean Doppler velocity ( $V_{\text{dop}}$ ) simulated using LESs are  
27 compared with 2-year measurements from a Radar Wind Profiler (RWP) as viewed by statistical  
28 composites separated according to wet and dry season conditions. In the observed RWP and  
29 simulated LES  $V_{\text{dop}}$  composites, we find more intense low-level updraft velocity, vigorous graupel  
30 generation, and intense surface rain during the dry periods than the wet periods. To investigate  
31 coupled updraft-microphysical processes further, single-day golden cases are selected from the  
32 wet and dry periods to conduct detailed cumulus thermal tracking analysis. Tracking analysis  
33 reveals that simulated dry-season environments generate more droplet-loaded low-level thermals  
34 than wet-season environments. This tendency correlates with seasonal contrasts in buoyancy and  
35 vertical moisture advection profiles in large-scale forcing. Employing a normalized time series of  
36 mean thermal microphysics, the simulated cumulus thermals appear to be the primary generator of  
37 cloud droplets. When subsequent thermals penetrate the ice crystal layer, droplets within the  
38 thermals interact with entrained ice crystals, which enhances riming in the thermals. This appears  
39 to be a production pathway of graupel/hail particles within simulated deep convective cores. In  
40 addition, less-diluted dry-case thermals tend to be elevated higher, and graupel grows further  
41 during sedimentation after spilling out from thermals. Therefore, greater concentrations of low-  
42 level moist thermals likely result in more graupel/hail production and associated dry-season  
43 convective vigor.

44

45 **1. Introduction**

46

47 Deep convection is a fundamental process of turbulence that drives the Earth's general circulation  
48 and regulates thermodynamic fields (Emanuel et al., 1994). Deep convection undergoes complex  
49 dynamical and microphysical processes throughout its life cycle, which appear as towering clouds  
50 visible from satellites in different parts of the world (Stephens et al., 2002). As a result, deep  
51 convection generates significant amounts of atmospheric latent heat, surface precipitation, and  
52 hydrometeors that reflect/absorb solar and infrared radiation, modifying atmospheric circulation  
53 and surface energy and mass fluxes (Hartmann, 2016). These complexities in deep convection and  
54 feedback processes pose significant challenges in predicting weather and climate using numerical  
55 Earth system modeling across different scales (Grabowski and Petch, 2009; Sullivan and Voigt,  
56 2021).

57

58 Characteristics of deep convection are unique in different seasons and geographic regimes affected  
59 by the local environment. One of the most straightforward yet most robust regime separation  
60 concepts is the land-ocean (L-O) contrast (Williams and Stanfill 2002). Solar radiation increases  
61 the surface skin temperature over land more readily than over the ocean due to the smaller heat  
62 capacity of soils and vegetation than deep water bodies, thus producing stronger surface infrared  
63 flux and turbulent heat flux (Matsui and Mocko 2014). This greater surface energy deepens  
64 planetary boundary layers that may trigger deeper convective clouds depending on the atmospheric  
65 profiles (Pielke 2001). Overall, the continental environment tends to promote deeper convection  
66 with stronger, wider convective cores (Lucas et al. 1994, Wang et al. 2019), with suppressed warm  
67 rain and enhanced cold precipitation process (Williams et al. 2005), which often leads to unique  
68 drop-size distribution characteristics and precipitation partitioning between convective and  
69 stratiform process outcomes in different geographic regions (e.g., Tokay and Short 1996;  
70 Giangrande et al. 2012; Dolan et al. 2018).

71

72 Satellite observations similarly depict continental convective invigoration as characterized by  
73 more frequent lightning flashes and heavily rimed particles aloft over land than ocean (Williams  
74 et al. 2004, Zipser et al. 2006, Stolz et al. 2015, Matsui et al. 2016). Takahashi et al. (2017 & 2021)

75 show that continental convection generally contains less diluted cores than their oceanic  
76 counterparts, following an inverse relationship between convective core width and dilution rate.  
77 Similarly, Jeyaratnam et al. (2020) recently suggested that convective updraft and mass flux  
78 properties were distinctly different between tropical land and tropical oceanic convection using  
79 methods to estimate those properties that blend satellite observations with plume models. Hereafter,  
80 we define “convective vigor” by the enhanced cold-precipitation process characterized by larger  
81 rimed particles (graupel/hail) and large and copious raindrops in convective cores.

82

83 Representation of deep convective cloud land-ocean contrasts is still an ongoing challenge for  
84 global atmospheric models at storm-resolving resolution (a few km of horizontal grid spacing),  
85 partially owing to the poor representation of cloud dynamics (Matsui et al. 2016). Robinson et al.  
86 (2011) configured idealized simulation setups to investigate the “island” effect of convection with  
87 finer grid spacing (500 m or 1 km) and successfully simulated convective vigor equivalent to the  
88 observed microwave brightness temperature. Matsui et al. (2020) used a nested regional model  
89 with 1 km grid spacing to compare mid-latitude continental versus tropical maritime storms and  
90 successfully reproduced land-ocean contrasts of hydrometeor identification profiles from  
91 polarimetric radars.

92

93 However, statistical evaluation of simulated vertical velocity and association with convective  
94 vigor process (i.e., graupel/hail generation) have not yet been examined very well due to a lack of  
95 observations and detailed process-oriented model investigation, respectively. For example,  
96 mesoscale convective system (MCS) studies performed by Prein et al. (2022) and Ramos-Valle et  
97 al. (2023) highlight the challenges when attempting to represent continental convection within the  
98 constraints of limited observations while attempting to establish optimal configurations as a  
99 function of model grid spacing for typical midlatitude (Oklahoma) and tropical continental  
100 (Amazon) conditions.

101

102 The 2-year measurements from the Green Ocean Amazon (GoAmazon) campaign provide  
103 unprecedented data on the vertical velocity of deep convection by the Atmospheric Radiation  
104 Measurement user facility (ARM, ARM Mobile Facility (AMF), Martin et al. 2017, Giangrande  
105 et al. 2017). Recently, Giangrande et al. (2023) contrasted the thermodynamics and lifecycle

106 properties, including the vertical air velocity within isolated convective clouds observed during  
107 the Amazon wet and dry seasons, and found that dry-season convection exhibited more intense  
108 low-level updrafts and larger reflectivity associated with smaller convective cell areas than wet-  
109 season counterparts. Dry-season convection also tended to exhibit a shorter life cycle and often  
110 achieved maximum updraft and precipitation intensity at earlier life cycle stages than wet-season  
111 storms. Pre-convective thermodynamics profiles from those events revealed that the dry season  
112 showed a stronger deficit of dew-point temperature in the middle troposphere and higher values of  
113 mean-layer convective available potential energy (MLCAPE) at lower levels.

114  
115 In addition to primary thermodynamic transitions between wet and dry season convective regimes  
116 (e.g., Giangrande et al. 2020), the Amazon dry seasons may experience larger concentrations of  
117 aerosols due to biomass burning that have been recently associated with potential secondary  
118 contributions to changes in storm precipitation properties and convective vigor (e.g., Lin et al.  
119 2006; Wang et al. 2018; Öktem et al. 2023). Moreover, the Amazon dry (wet) season has long  
120 been suggested to promote a continental (maritime) convection contrast for a given  
121 thermodynamic profile and background aerosols (Williams et al. 2002). Typical land-ocean  
122 contrast is characterized by a “hot” continental surface (Williams and Stanfill 2002) and sea-breeze  
123 type of mesoscale dynamics due to the thermal-patch effect (Robinson et al. 2011). Thus, instead  
124 of focusing on the complex nature of land-ocean contrast or other active versus break monsoonal  
125 contrasts performed globally (e.g., Holland et al. 1986, Keenan and Carbone 1992, Pope et al.  
126 2009, Wu et al. 2009), the dry-wet season contrasts over the Amazon basin allows a unique  
127 emphasis on the impact of thermodynamic profiles and large-scale dynamics upon the formulation  
128 of convective vigor.

129  
130 The main objective of this paper is to investigate dry-wet seasonal contrast and potential changes  
131 in the evolution of deep convection cloud processes using an LES model and forward simulations  
132 of Doppler radar observations. This attempts to reveal dynamical and microphysical processes that  
133 explain the observed dry-wet contrasts, focusing on the bulk controls imposed by the background  
134 thermodynamic profiles and large-scale forcing. The motivation for these efforts is the argument  
135 that an improved understanding of these dry-wet contrasts should facilitate untangling the more  
136 complex processes of land-ocean contrasts in deep convection. For this study, we employ a series

137 of daily large-eddy simulations (LESs) with bulk single-moment microphysics throughout the  
138 GoAmazon campaign dry and wet season intensive observation periods (IOPs) to characterize dry-  
139 wet season contrast in convection. These simulations are validated against the cumulative statistics  
140 of ground-based Doppler velocity measurements during those periods. A thermal tracking analysis  
141 is conducted to select golden cases from these dry- and wet-season LES runs to investigate the  
142 physical process of convective vigor further. This effort focuses on thermodynamic impacts and  
143 cloud dynamical roles in this manuscript, while the aerosol effects will be investigated in another  
144 study.

145  
146 Section 2 describes the general methodology and tools, including radar profilers, LES,  
147 instrumental simulators, large-scale meteorological forcing, and thermal-tracking algorithms for  
148 this study. Section 3 shows the results of the dry-wet contrast of meteorological forcing, statistical  
149 composites of Doppler velocity, and thermal tracking analysis. Section 4 summarizes a thermal-  
150 driven process of dry-season convective vigor, its uncertainties, and future directions.

151

152

## 153 **2. Methods**

154

### 155 **2.1 GoAmazon: RWP Observations**

156

157 The primary datasets for this study are those collected by the 1290 MHz ARM Radar Wind Profiler  
158 (RWP) operated during the U.S. Department of Energy’s ARM facility deployment during  
159 its “Observations and Modeling of the Green Ocean Amazon 2014–2015” (GoAmazon) campaign  
160 near Manaus, Brazil, from March 2014 through December 2015 (e.g., Martin et al., 2017). The  
161 RWP was configured for precipitation sampling that included frequent vertical pointing to collect  
162 conventional radar reflectivity factor  $Z$  and mean  $V_{\text{dop}}$  profiles through deep convective cells to  
163 approximately 17 km in altitude (e.g., Giangrande et al. 2013, Giangrande et al. 2016, Wang et al.  
164 2019, Williams et al. 2023). For measurements collected at these ultra-high frequencies and  
165 without expectations for larger hail in Amazon deep convective storms (Liu and Zipser 2015, Bang  
166 and Cecil 2019), all radar estimates are assumed as within Rayleigh scattering regimes, and  
167 measurements are unattenuated in rain. The RWP deployed during GoAmazon had a beam width

168 of approximately 10 degrees thus horizontal measurement resolution is typically less than 1 km,  
169 with a 200 m vertical (bin, gate) resolution and 10-s intervals between consecutive radar profiles.  
170 All radar measurements were calibrated against a reference laser disdrometer collocated at the  
171 main AMF site during the campaign (e.g., Wang et al. 2018), and a detailed method is discussed  
172 in Williams et al. (2023).

173

174 For observation and simulation comparisons, the deep convective core is defined by using  
175 thresholds applied to the observed and simulated RWP profiles: 1) column-maximum reflectivity  
176 is greater than 35 dBZ, and 2) column-maximum  $V_{\text{dop}}$  is greater than 5 m/s. The choice for these  
177 criteria is admittedly flexible, as model-vs-observed Z thresholds, in particular, are not necessarily  
178 well-posed for convective-stratiform segregation such as removing all stratiform cells (e.g., Steiner  
179 et al. 1995). Still, the additional velocity constraint afforded by the vertically-pointing RWP and  
180 statistical representation of convective and stratiform composites seems to be reasonable (not  
181 shown here), noting what is important is an attempt to apply thresholds for both observations and  
182 simulations. A slightly different threshold does not alter the conclusions. Note that events on  
183 3/19/14, 3/20/14, and 3/23/14, as well as the 10/4/14 cases from the dry season IOP, are clear  
184 examples of Amazon mesoscale convective systems (MCSs, e.g., Wang et al. 2019). Thus, these  
185 cases have also been removed from our statistical analysis to focus on isolated convective days.

186

187

## 188 **2.2 GoAmazon LES, Forcing, and Simulator**

189

190 GoAmazon LES runs utilize the Goddard Cumulus Ensemble (GCE), a cloud-process model  
191 developed and improved at NASA GSFC over several decades (Tao *et al.* 2014). The GCE is  
192 driven by large-scale forcing (LSF) with cyclic boundary conditions to generate cloud dynamics  
193 and microphysics processes in Cartesian grid coordinates. No additional heat, moisture, or  
194 momentum enters the domain apart from that imposed by the LSF or solar/infrared radiative  
195 processes. In addition, GCE's anelastic dynamic core option allows faster integration of finer-  
196 resolution runs (up to 1.5~2 times) than its compressible dynamic core option.

197

198 GoAmazon LES runs use 200-m horizontal grid spacing with 512 x 64 x 128 grids (x-y-z cartesian  
199 coordinates) with a 2-second model time step. Vertical grid spacings stretch from near surface  
200 level (starting from 44 m) and reach 200m around 4 km level, not to exceed horizontal resolution.  
201 Thus, the domain covers a 102 km x 12.8 km area; this “narrow channel” domain setup intends to  
202 resolve three-dimensional large eddies (i.e., thermals) while minimizing computational cost in  
203 order to run LES for the entire IOPs. In terms of model physics, the 1.5-order turbulent kinetic  
204 energy (TKE) scheme is used for subgrid turbulent mixing, and the Goddard radiation scheme is  
205 used for computing radiative flux and heating (Chou and Suarez 1999 & 2001, Matsui et al. 2018).  
206 The Goddard bulk one-moment 6-class scheme (4ICE hereafter) has four ice classes and uses  
207 preset size and density mapping for snow, graupel, and hail (Lang et al. 2014; Tao et al. 2016).  
208 4ICE successfully generated a realistic L-O contrast of convective-core hydrometeor distributions  
209 compared to polarimetric radar retrievals in the previous study (Matsui et al. 2020). Also, note that  
210 the one-moment scheme is unaffected by the background aerosol concentrations to focus on the  
211 impact of thermodynamic and large-scale forcing on convective vigor in this study.

212  
213 The LSF is derived from the VARIational ANALysis (VARANAL) approach, which is a broadly  
214 accepted method for generating large-scale forcing wherein data are collected and adjusted based  
215 on the vertical integration of the atmospheric mass, moisture, dry static energy, and momentum  
216 budgets (Zhang and Lin 1997, Zhang et al. 2001, Xie et al. 2004). The VARANAL approach is  
217 applied to the GoAmazon field campaign using ERA-Interim reanalysis (Dee et al., 2011) and  
218 constrained by radar-based surface precipitation rate (Tang et al. 2016). The horizontal/vertical  
219 advective forcings, mean wind profiles, and surface heat fluxes from the GoAmazon LSF are used  
220 to drive the LES. These fields are interpolated and imposed as tendency terms at every model time  
221 step. Our previous research demonstrated that GCE reproduced the observed precipitation quite  
222 well when forced by the GoAmazon LSF (Tao et al. 2022). GoAmazon LESs are run from  
223 September 2014 to 10 October 2014, defined as the dry-season IOP, and also run from 14 February  
224 2014 to 26 March 2014, defined as wet-season IOP, as suggested by thermodynamic behaviors  
225 characteristic of larger dry and wet-season expectations, respectively (Giangrande et al. 2017,  
226 2020). Each daily LES is initialized at 12 AM local time from the LSF and integrated just for 30  
227 hours rather than continuously integrated during the entire IOPs because the convection life cycle  
228 typically follows a strong diurnal cycle due to the solar heating cycle, excepting propagating



229 organized convection (Tang et al. 2016, Giangrande et al. 2017, 2020). As a default setting, hourly  
230 LES outputs are used to analyze the mean seasonal behavior of LESs.

231  
232 Hourly LES outputs include an additional Doppler velocity field, corresponding to an expected  
233 RWP observation through a multi-instrumental simulator, Goddard Satellite Data Simulator Unit  
234 (G-SDSU, Matsui et al. 2014a; Matsui et al. 2014b). In this study, a ground-based Doppler radar  
235 simulator is implemented in the model to replicate RWP observable signals. Radar backscatter is  
236 estimated from non-Rayleigh calculations with a Maxwell-Garnett assumption of air-water-ice  
237 mixtures at 1290 MHz frequency, though for the RWP frequency, vertical pointing, and media  
238 type/size expectations therein, the forward modeling is more straightforward than most weather  
239 radar wavelength applications and appropriate for Rayleigh scattering assumptions. Doppler  
240 velocity is estimated using pressure-adjusted hydrometeor terminal velocities weighted by radar  
241 backscatter spectrum for each particle size distribution (PSDs). All these single scattering  
242 calculations follow the 4ICE microphysics calculation/assumptions of particle size, density, and  
243 phase for each hydrometeor species for physics consistency (Matsui et al. 2014b). Finally,  
244 simulated signals are averaged consistent with the RWP beamwidth (10 degrees). This beamwidth  
245 implies different averaging at different heights, for example, corresponding to six horizontal grids  
246 of the LESs being averaged for a representative output at the 15 km height. Overall, this beamwidth  
247 averaging smear LES-scale Doppler velocity signal statistics closer to the anticipated observed  
248 instrumental signals (Matsui et al. 2014b). However, it should be noted that the exact sampling  
249 methods are different between observations and simulations. For example, the RWP observations  
250 are vertical pointing measurements that collect profiles at 6-second (“instantaneous”) intervals. In  
251 contrast, the modeled RWP signals are drawn from a domain-wide sampling of hourly LES outputs.

252

253

### 254 **2.3 Thermal Tracking Algorithm**

255

256 The thermal tracking method used here is described in detail by Hernandez-Deckers and Sherwood  
257 (2016), who improved the initial version used by Sherwood et al. (2013). It is an offline algorithm  
258 that uses high temporal resolution output (~1 min) from LES to identify and track coherent rising  
259 volumes of cloudy air, i.e., thermals. The algorithm first identifies all peak vertical velocities larger

260 than 0.8 m/s that have water condensate content of at least 0.01 g/kg at every available snapshot  
261 of the simulation and matches peaks from successive snapshots to identify the available points of  
262 the trajectories of rising cloudy air parcels. A third-order polynomial is fitted to these points to  
263 reconstruct smooth trajectories and to allow a precise estimate of the ascent rate of the rising air  
264 volume at each snapshot. Notice that this ascent rate differs from the actual vertical velocity at a  
265 particular grid point since thermals develop internal toroidal circulations such that the peak vertical  
266 velocity at their centers is higher than the actual ascent rate of the air volume (e.g., Blyth et al.  
267 2005; Sherwood et al. 2013).

268  
269 The extent of each rising air volume (the size of each thermal) is estimated assuming a spherical  
270 shape centered at its smoothed trajectory, ensuring that the average vertical velocity of the enclosed  
271 volume matches that obtained from the derivative of the trajectory. Tracked thermals must fulfill  
272 certain requirements; for example, they must be tracked for at least three time steps, their radius  
273 must be larger than twice the horizontal grid spacing, their time-average ascent rate must be at  
274 least 1 m/s, their change in size in between successive snapshots must be less than 80% of the  
275 smallest radius, and most importantly, their trajectories must be consistent with their vertical  
276 momentum budget. The momentum budget of a tracked thermal is computed from its buoyancy  
277 (obtained from the density field), the pressure gradient force (obtained by integrating the pressure  
278 field over the entire thermal's surface), a "resolved mixing term" (obtained from the convergence  
279 of vertical momentum flux across the thermal's surface), and an entrainment or detrainment  
280 contribution due to the change in size between snapshots. This allows us to compute the expected  
281 final position of each thermal based only on its initial ascent rate, which is compared with the  
282 thermal's last tracked position. The distance between the actual and expected final positions must  
283 be smaller than the average thermal diameter and smaller than 20 % of the vertical distance  
284 traveled; otherwise, the thermal is discarded.

285  
286 Once thermals are tracked with this algorithm, many properties can be studied based on all  
287 available model variables of interest. For example, average values for each thermal, such as ascent  
288 rate, size, altitude, entrainment rate, etc., are easily computed. Also, composites of different  
289 quantities can be obtained for different "stages" of a thermal's lifecycle. Typically, thermals exhibit  
290 one maximum ascent rate throughout their lifetime, which indicates their most vigorous phase.

291 This time step is used as a time reference common ( $t=0$ ) to all thermals to create composites of  
292 various properties at different stages of thermal lifetimes. Note that our tracking algorithm cannot  
293 analyze merging or splitting thermals, regardless of their occurrence. This limitation requires  
294 further study.

295

296 This thermal tracking algorithm was first used to study the main properties of cumulus thermals in  
297 simulations of transient-growing convection (Sherwood et al., 2013; Hernandez-Deckers and  
298 Sherwood, 2016) and provided strong evidence that thermals are typically small, short-lived (4-5  
299 minutes on average), and mix vigorously with their environment. Also, Hernandez-Deckers and  
300 Sherwood (2016) showed that the spherical shape approximation is generally valid and that  
301 thermals, rather than plumes, are a more realistic building block for cumulus clouds. Hernandez-  
302 Deckers and Sherwood (2018) used this algorithm to study the mixing properties of thermals in  
303 more detail and contrast them with known parameterizations. Results from these studies have set  
304 up the stage for a deeper understanding of cumulus dynamics and for further studies that use  
305 different approaches (e.g., Gu et al., 2020; Morrison et al., 2020; Peters et al., 2020; Xu et al.,  
306 2021; Morrison et al., 2023). Recently Hernandez-Deckers et al. (2022) used this algorithm to  
307 study aerosol-deep convection interactions, highlighting the importance of the strong coupling  
308 between microphysics and small-scale dynamics in convective clouds. Here we run this tracking  
309 algorithm with the GCE model output for 5 hours starting at 1900Z (3 pm local time) on 09/07/14  
310 (dry case) and 02/26/14 (wet case), using 1-minute interval output.

311

312

### 313 **3. Results**

314

#### 315 **3.1 Dry-Wet Contrast of Large-Scale Forcing**

316 Campaign atmospheric thermodynamic profiles and the typical variability observed during  
317 GoAmazon dry and wet seasons have been previously depicted using composite radiosonde skew-  
318 T log-P diagrams (e.g., Giangrande et al., 2017, 2020, 2023). These depictions often show very  
319 similar temperature profiles between dry and wet seasons, whereas the moisture profiles indicate  
320 apparent differences, highlighting the mid-level deficit of the dew-point temperature profile in dry-

321 season composites. Since this study utilizes LSF to drive LESs, seasonal thermodynamics and  
322 dynamics are re-characterized by the LSF (Tang et al. 2016).

323

324 In Fig. 1, we plot a time series of apparent moisture sinks ( $Q_2$ ), vertical moisture advection, and  
325 parcel potential buoyancy profiles with surface precipitation rate from GoAmazon LSF for the  
326 IOPs. These time series of LSF profiles are integrated and contrasted in terms of Contoured  
327 Frequency by Altitude Diagrams (CFADs, Yuter and Houze 1995) as the dry and wet season IOPs  
328 (Figure 2).

329

330 Here,  $Q_2$  is the sum of changes in moisture content, horizontal moisture advection, and vertical  
331 moisture advection (Yanai et al. 1973), balanced with net condensation rate and turbulent transport  
332 of moisture vertical advection. Large  $Q_2$  corresponds to a large atmospheric moisture loss due to  
333 net condensation loss (i.e., precipitation). Large  $Q_2$  is associated with intervals with heavier or  
334 more widespread surface precipitation; thus, dry-IOP  $Q_2$  and surface precipitation are typically  
335 smaller than wet IOP (Fig. 1a-b). Similarly, Figs. 1c-d shows that peaks of vertical moisture  
336 advection term coincide with those peaks in the  $Q_2$  rate. Note that the  $Q_2$  rate in tropical  
337 environments is mainly contributed by the vertical moisture advection term rather than the  
338 horizontal advection term (not shown here). More importantly, positive (red shade) vertical  
339 moisture advection of the wet IOP tends to be stretched up to higher altitude (up to 200 mb) than  
340 the dry IOP (up to 600 mb) in most cases.

341

342 As previously discussed by Tang et al. (2016), the associated Amazon  $Q_2$  CFADs show the largest  
343 positive  $Q_2$  between 700 and 400 mb, while the largest negative  $Q_2$  is around 800 mb (Figs. 2a-  
344 b). The Dry-wet composite CFAD highlights more frequent positive  $Q_2$  values above the 800 mb  
345 level during the wet IOP. In contrast, more frequent negative  $Q_2$  during the dry IOP (Fig. 2c).  
346 Vertical moisture advection depicts similar CFAD shapes (Figs. 2d-e). Still, it highlights high  
347 frequencies of low-level positive vertical moisture advection and mid-to-low-level negative  
348 moisture vertical advection in the dry IOP in comparison with the wet IOP.

349

350 Finally, in Figs. 1e-f we plot the time series of parcel potential buoyancy profiles (positive  
351 components only), computed from LSFs by lifting surface airmass dry and moist adiabatically.

352 These potential buoyancy magnitudes are not necessarily associated with precipitation intensity.  
353 Potential buoyancy CFADs show peak forcing between the 600 mb and 200 mb levels (Figs. 2g,  
354 h, & i). The wet IOP suggests a larger variability of potential buoyancy at the upper troposphere  
355 than the dry IOP (Figs. 2g-h). Potential buoyancy appears to be slightly stronger in the dry IOP,  
356 and concentrated in a relatively lower troposphere than its wet IOP counterpart (Fig. 2i), which  
357 agrees with findings in Giangrande et al. (2023). These results will be further discussed along the  
358 thermal concentrations in the latter section.

359

360

### 361 **3.2 Dry-Wet Composite of Doppler Velocity CFADs**

362

363 Giangrande et al. (2023) highlighted dry-wet seasonal characteristics of storm vertical air motions  
364 retrieved using RWP. They found that daytime isolated dry season convective cells tend to have  
365 stronger updrafts at altitudes below the melting level. Yet, unlike their wet-season counterparts,  
366 updrafts do not increase in intensity much above the melting layer. However, dry-season  
367 convective cores were also characterized by stronger downdrafts at all altitudes, especially when  
368 compared to wet-season counterparts aloft. Our present study utilizes similar direct measurements  
369 of the mean  $V_{\text{dop}}$  from RWP to characterize the dry-wet contrast of deep convective cores. The  
370 advantage of using  $V_{\text{dop}}$  measurements is that the quantity is the direct radar measurement and  
371 helps reduce uncertainties from retrieval assumptions, such as requiring hydrometeor  
372 identification or associated terminal fall speed corrections if the intent was to retrieve the vertical  
373 air motion (Giangrande et al. 2013, 2016). Here, vertically-pointing  $V_{\text{dop}}$  measurements contain  
374 sufficient information to evaluate storm characteristics, with the understanding that these  
375 measurements represent the terminal velocities of hydrometeors combined with the vertical air  
376 motion.

377

378 In Fig. 3a, we provide the cumulative sample numbers of CFADs (for each bin of  $V_{\text{dop}}$  and altitude)  
379 as simulated and subsampled from the LES hourly outputs from the combined dry and wet season  
380 IOPs. If the sampling numbers are normalized for each altitude, the  $V_{\text{dop}}$  CFADs will be formed.  
381 Fig. 3b shows the sum of hydrometeor mass concentrations from each  $V_{\text{dop}}$ -altitude bin. Namely,  
382 each hydrometeor mass concentrations from “cloud”, “rain”, “graupel-plus-hail”, or “ice-plus-

383 snow” are separately accumulated for each bin. The larger number of samples associated with a  
384 larger accumulated mass concentration of hydrometeor can generate the “representativeness” of  
385 the hydrometeor class for a given  $V_{\text{dop}}$ -altitude bin location. Because  $V_{\text{dop}}$  is the sum of the vertical  
386 velocity of the air and the terminal velocity of hydrometeor particles weighted by their reflectivity,  
387 this plot facilitates understanding  $V_{\text{dop}}$  CFAD.

388

389 As mentioned above, we defined four regimes based on the accumulated mass of each hydrometeor  
390 category. The “cloud” category (CL) is centered around -5 m/s of  $V_{\text{dop}}$  and 4 km altitude, slightly  
391 overlapping with other categories. A “rain” category (RA) is more narrowly concentrated around  
392 -8 m/s of  $V_{\text{dop}}$  and below 4 km altitude. The “graupel-plus-hail” category (GH) is centered around  
393 -14 m/s of  $V_{\text{dop}}$  at 5 km altitude. Finally, an “ice-plus-snow” category (IS) is narrowly concentrated  
394 along -1 m/s of  $V_{\text{dop}}$  above 5 km altitude. These locations roughly correspond to each hydrometeor  
395 category's altitude and terminal velocity when factoring in the background/ambient vertical air  
396 velocity. Note that our “cloud” regime has no terminal velocity in GCE 4ICE microphysics, thus  
397  $V_{\text{dop}}$  represents or tracks the background vertical air velocity and overlaps with the other regimes.  
398 Moreover, simulated  $V_{\text{dop}}$  and hydrometeor statistics are also sensitive to model physics and those  
399 assumptions to some degree. For example, any real-world cloud regime may be extended to higher  
400 altitudes, but the model 4ICE microphysics scheme tends to quickly convert cloud liquid to cloud  
401 ice category due to saturation adjustment (See Figs. 14-16 of Matsui et al. 2023). Nevertheless,  
402 this representative mapping will help discuss the variability of the  $V_{\text{dop}}$  CFADs between the dry  
403 and wet season IOPs.

404

405 In Fig. 4, we provide an observed and simulated climatology of  $V_{\text{dop}}$  CFADs as sampled from deep  
406 convective cores and summarized over the dry and wet season IOPs. In both the dry and wet season  
407 IOPs, the observed CFADs depict a smoother transition of the  $V_{\text{dop}}$  at the freezing level into the  
408 melting layer (4-5 km, Figs. 4a-b). At the same time, simulations show a more abrupt transition  
409 around the freezing layer (Figs. 4d-e). This is primarily because bulk single-moment microphysics  
410 more abruptly converts solid to liquid phases through autoconversion than explicit bin-resolving  
411 microphysics (Iguchi et al. 2014). This rapid conversion also overestimates the terminal velocity  
412 of raindrops near and just below the freezing level. Another possible reason is overestimating the  
413 graupel/hail size, leading to larger melted raindrops with high terminal velocity.

414

415 The CFADs have been summarized according to dry and wet season IOPs to explore these seasonal  
416 contrasts between the deep convective cores (Figs. 4c, 4f). In the R regime (green box), the dry  
417 IOP suggests more prevalent samples in strongly negative  $V_{\text{dop}}$  for our observations and  
418 simulations, indicating that deep convective cores during the dry season IOP tend to have more  
419 vigorous, faster-falling (larger) raindrops. In the GH regime (purple box), the dry season IOP  
420 dominates the sampling. The observations indicate this dominance (red shade) up to 10 km altitude  
421 (the extent that observations were included), while the simulation shows this behavior up to 8 km,  
422 suggesting LES underestimation in graupel/hail altitudes. In the CL regime, the observations and  
423 the simulations agree well, except that some sampling is overwhelmed by the dry season IOP  
424 behaviors in the overlapped area. This likely indicates a shift in the presence of stronger low-level  
425 updraft velocities, consistent with the analysis in Giangrande et al. (2023).

426

427 When considering the IS regime, there are examples of agreements and discrepancies between the  
428 observations and simulations. One key agreement is that the wet IOP dominates the samples in the  
429 area of positive  $V_{\text{dop}}$  above 8 km altitude. This indicates that observations and simulations suggest  
430 a shift towards stronger upper-level vertical air velocity for the wet season IOP examples than for  
431 the dry season IOP. This is consistent with the absence of dry mid-levels and the stochastic updraft  
432 model expectations from Giangrande et al. (2023). On the other hand, the observations indicate a  
433 more dominant sampling of velocities during the wet season IOP at around -3 m/s of  $V_{\text{dop}}$ , whereas  
434 simulations change the dominant sampling mode from wet to dry IOPs at around 7 km altitude.  
435 This is a potential bias in single-moment bulk microphysics, which tends to glaciate cloud droplets  
436 or raindrops more quickly into ice particles than double-moment schemes (e.g., Fig. 16 of Matsui  
437 et al. 2023). The observed composite also shows more dry-season dominant frequencies in GH  
438 zones than the simulation, indicating the underestimation (overestimation) of raindrop/graupel  
439 (ice/aggregate) particles above 7 km height.

440

441 Excepting this discrepancy in the IS regime, dry-wet composites of  $V_{\text{dop}}$  CFAD agree well between  
442 observations and simulations, suggesting that LES could successfully represent the important  
443 nature of dry-wet contrast, i.e., dry-season convection tends to generate stronger low-level updraft

444 velocity, generating more graupel/hail, and vigorous raindrops accompanied with stronger low-  
445 level downdraft than the wet season.

446

447 To further investigate these seasonal shifts in core properties, golden cases are selected to analyze  
448 deep convection lifecycle and processes. Golden cases are two single-day simulation cases, one  
449 for dry and one for wet season, representing  $V_{\text{dop}}$  CFADs of each season. For this, the  $V_{\text{dop}}$  CFADs  
450 are constructed for each day during the wet and dry season IOPs, and these daily CFADs are  
451 compared to the composites of seasonal CFADs (not shown here). After day-to-day analysis of  
452 correlation and root-mean-square errors between daily and seasonal CFADs, the convective event  
453 on the 2/26/14 case is selected to represent the wet IOP convections. In contrast, the 9/7/14 case is  
454 chosen to represent dry IOP convection. Fig. 5 shows a dry-wet composite of  $V_{\text{dop}}$  CFAD using  
455 these two case studies. This figure compares quite well with the seasonal composite of  $V_{\text{dop}}$  CFAD,  
456 having the dry convective vigor signals and model biases of the seasonal composite (Fig. 4f).

457

458 In Fig. 6, we show a time series of domain-mean profiles of convective cores drawn from these  
459 dry- and wet-season golden cases, highlighting from 1600Z (1200 local time) of the starting day  
460 to 0400Z (0000 local time) of the next day. The dry season golden event shows a clear diurnal  
461 convection cycle, peaking at 2100-2200Z (local 5-6 pm). In contrast, the wet season golden event  
462 shows an already ongoing, continuous sequence of deep convection with several embedded strong  
463 pulses. Convective top heights reach up to 17 km for both the dry and wet events (Figs. 6a-b).  
464 Low-level positive upward vertical velocity is more ubiquitous in the dry case, while upward  
465 vertical velocity of the wet case extends to the middle-to-upper troposphere up to 15km (Figs. 6c-  
466 d).

467

468 Dry-case graupel-plus-hail (GH) mass concentrations peak around 2100-2300Z when the  
469 convective clouds reach their deepest cloud top heights, and the maximum GH concentration  
470 exceeds that of the wet case. Rain mass concentrations peak between 2200Z and 00:30Z on the  
471 subsequent day for the dry case, and this appears to be slightly more intense than the rainfall  
472 simulated for the wet cases. Note that precipitation areal fraction is expected to be larger for the  
473 wet season (i.e., Giangrande et al. 2016, 2023), such that dry-season convection is often  
474 characterized by narrow yet intense isolated convection, while wet-season convection is



475 characterized by widespread moderate to deep convection (although with higher domain mass  
476 flux). The intense surface rainfall rates are generally correlated with the generation of graupel,  
477 frozen drops, and/or small hail particles during the dry-season convection, but there are some time  
478 lags from 21Z to 22:50Z in the dry-case convection. This is because the initial convective core is  
479 much narrower, and near-surface relative humidity is slightly low (~80%) around 21Z, and later  
480 convective area increases so as near-surface relative humidity (~96%) around 21:50Z. Thus, more  
481 surface rain evaporation likely suppresses surface precipitation during earlier convective periods.  
482 These time series behaviors are generally consistent with the observed characteristics in the time-  
483 integrated  $V_{\text{dop}}$  CFADs (Fig. 5).

484

485 One key question is why larger or heavily rimed particles tend to be preferentially generated in  
486 dry-season convection compared to wet-season convection, given that both seasons indicate  
487 convection with intense updraft velocity. This question follows previous efforts of Williams and  
488 Stanfill (2002) for simulations of deep convection that contrasted land and oceanic clouds. For  
489 example, while land and ocean environments may have similar convective available potential  
490 energy (CAPE), differences in detailed potential buoyancy and vertical velocity profiles enable  
491 additional graupel/hail particles to form in continental deep convection when compared to the  
492 maritime environments (Matsui et al. 2020). A Lagrangian tracking analysis is performed to  
493 examine this question for Amazon dry and wet season contrasts to investigate the dynamics and  
494 microphysics within cumulus thermals for these dry and wet golden events (Section 3.3).

495

496

### 497 **3.3 Thermal Tracking Analysis**

498

499 Thermal tracking analysis (Section 2.3) was conducted over 5-hour periods from 1900Z to 0000Z  
500 for the dry and wet season events using 1-minute LES outputs. Fig. 7 depicts normalized x-z cross-  
501 sections of thermal properties at the moment of maximum vertical velocity in the dry and wet cases  
502 and dry-wet differences. Thermals typically experience development and decaying stages in their  
503 lifetime. During development, moist thermals increase their vertical velocity and size by releasing  
504 latent heat and entraining surrounding air (Morrison et al. 2021). After defining and tracking each  
505 thermal from the LESs, our normalizing procedure first defines the reference time from each

506 thermal's lifetime based upon peak vertical air velocity (denoted as thermal maxima) and then  
507 conducts a weighting average of each thermal property at the thermal maxima only. Our weights  
508 are based on the magnitude of thermal mass flux to avoid under-representing properties of less-  
509 populated but vigorous thermals. Because these heights at thermal reference time are different for  
510 each thermal in dry and wet case studies, averaging properties are somewhat biased toward thermal  
511 vertical distributions (discussed later).

512  
513 For example, in Fig. 7a we plot the weighted-average peak vertical air velocity ( $W$ ) for the dry-  
514 case thermal (9.6 m/s) and the wet-case thermal (10.6 m/s). Perhaps surprisingly, the flux- and  
515 radius-weighted average dry-case thermal is slightly slower in  $W$  than that found for the average  
516 wet-case. Here, we find that the vertical air velocity of the wet-case thermal is more  
517 homogeneously distributed than its counterpart for the dry-case thermal, leading to higher  
518 weighted-mean  $W$  despite weaker values at thermal centers (red shade in Dry-Wet plot, Fig. 7a).  
519 Also, unexpectedly, supersaturation and cloud droplet mixing ratio ( $Q_c$ ) of the dry-case thermal  
520 are elevated compared to the wet-case thermal (Fig. 6b-c), since wet-case thermals may be  
521 expected to instead have higher supersaturation and/or more condensation owing to the higher  
522 availability of water vapor (e.g., Giangrande et al. 2023).

523  
524 Exploring the other classes, the rain mixing ratio ( $Q_r$ ) is similar between the dry-case and wet-case  
525 thermals (0.17 g/kg), but graupel-hail concentrations ( $Q_{g+h}$ ) are significantly larger in the dry-  
526 case thermals (0.95 g/kg) compared to the wet-case thermals (0.79 g/kg); this latter result is  
527 consistent with previous discussions from event time-series in Fig. 6e. Cloud ice and snow mixing  
528 ratio ( $Q_{i+s}$ ) values are slightly larger in the wet-case thermal (3.5 g/kg) than in the dry-case thermal  
529 (3.2 g/kg). While this difference is not significant, this is also potentially a surprising outcome  
530 since dry-case deep convective clouds might otherwise be expected to be deeper/stronger and thus  
531 characterized by additional ice hydrometeor concentrations. However, some absence of these  
532 media may be partially explained by following Giangrande et al. (2020; 2023) suggestions that  
533 drier mid-to-upper levels in the dry season may limit periphery precipitation aloft (i.e., enhanced  
534 evaporation). Overall,  $Q_r$  and  $Q_{g+h}$  seem to be concentrated in these composite averages  
535 downward from the thermal core due to the gravitational sedimentation process. Supersaturation  
536 and  $Q_c$ , however, are also more vertically elongated than thermal properties established by

537 Hernandez-Deckers et al. (2022) using the Weather Research and Forecasting (WRF) model for a  
538 case of scattered convection over Houston, Texas.  $Q_{i+s}$  is more homogeneously distributed across  
539 the defined borders of thermals. Also, dry-wet differences show slight asymmetric results,  
540 particularly in  $W$ ,  $Q_r$ , and  $Q_{g+h}$ . These could be attributable to differences in horizontal wind  
541 shear, evidenced by a greater tilt in the thermal centerline flow in the dry case (gray streamlines),  
542 leading to greater concentrations in the tilt direction of more rapidly sedimenting quantities that  
543 are formed within thermals (i.e.,  $Q_r$  and  $Q_{g+h}$ ); since thermal composites are not aligned with the  
544 mean wind, such preferential outflow may not be fully captured by this analysis (i.e., asymmetric  
545 signatures could be greater or lesser along other directions than X alignment).

546

547 An initial leading question is why the dry-case thermals have greater cloud water and  
548 supersaturation on average. To further untangle these results in Fig. 7b-c, we derive the vertical  
549 profiles of flux-weighted mean thermal states, now including all thermal times (Fig. 8a-g).  
550 Immediately, these plots reveal striking differences between the thermal number concentration  
551 ( $N$ ) profiles for dry-case and wet-case examples (Fig. 8a; the number of thermals per km height  
552 within the 102 km x 12.8 km domain). For instance, dry-case convection shows a larger  
553 concentration of thermals below the 8 km height, while wet-case convection promotes a more  
554 homogeneous thermal concentration that extends across most heights. This behavior is somewhat  
555 reminiscent of the distribution for the difference in vertical moisture advection and potential  
556 buoyancy profiles between the parent dry and wet season conditions (e.g., Fig. 1 and 2, discussions  
557 in Section 3.1). Moreover, thermal generation in our LES responds to these terms partially from  
558 the seasonal large-scale forcing.

559

560 According to the classic similarity theory of Morton et al. (1956), the width of dry/moist thermals  
561 should increase with increases in the boundary layer depth (William and Stanhill 2002). For the  
562 Amazon basin, previous GoAmazon studies such as Giangrande et al. (2017, 2023) showed that  
563 dry season boundary layer height is generally deeper than that of the wet season, potentially on the  
564 order of 200 m deeper for isolated deep convective events they tracked. Following this logic, dry-  
565 case convection may anticipate larger thermals. However, LES thermal tracking analysis suggests  
566 that the sizes ( $R$ ) of thermals upon initiation appear to be quite similar between the wet and dry  
567 events and then appear to grow at similar rates for several km before the dry-case thermal size

568 catches up with the moist size around 6 km in height, only to be overtaken again by the deeper  
569 wet-case thermals around 9 km (Fig. 8b). Further, Fig. 8c shows the mean vertical velocity of  
570 thermals, showing nearly identical updraft velocity below 4 km. However mean updraft velocity  
571 profiles above 4 km are quite different between the dry and wet cases; e.g., the dry case peaks  
572 around 8 km, while the wet case peaks at 6 and 10 km. This result implies that differences in moist  
573 convection between dry and wet cases are poorly characterized by thermal sizes.

574

575  $Q_c$  in thermals also shows very similar profiles between the dry and wet cases (Fig. 8d). However,  
576 because thermal numbers of the dry case are more concentrated at the lower troposphere (Fig. 8a),  
577 all-height mean properties of dry-case thermals are characterized by more  $Q_c$  (Fig. 7c).  $Q_r$  of the  
578 wet case is nearly twice as large as the dry case (Fig. 8e); however, normalized x-z cross-section  
579 (Fig. 7d) does not show such a large difference (explained below).  $Q_{i+s}$  also shows similar  
580 distributions (Fig. 8f). Still, total x-z mean  $Q_{i+s}$  is larger in the wet case than the dry case due to  
581 larger thermal numbers in the upper troposphere (Fig. 7e). Uniqueness appears in thermal  $Q_{g+h}$   
582 (Fig. 8g). While both dry and wet cases show similar magnitude of the peak values ( $\sim 0.9$  g/kg),  
583 the peak height in the dry case is approximately 3 km higher than the wet case. This  $Q_{g+h}$  peak of  
584 the dry case coincides with the peak of vertical velocity (Fig. 8c).

585

586 Fig. 8h-k displays these hydrometeor mixing ratios averaged over the same periods, including all  
587 convective grids defined by vertical velocity greater than 1 m/s. Vertical profiles and dry-wet  
588 differences are similar to the results in Fig. 6. However, compared with the in-thermal profile  
589 results (Fig. 8d-g), it facilitates understanding of the convective core microphysics process. First,  
590 mean in-thermal convective-grid hydrometeor concentrations are smaller than in-thermal profiles;  
591 particularly in-thermal  $Q_c$  values are roughly six times larger than convective-grid average  $Q_c$   
592 (Figs. 8d & 8h), suggesting that thermals are major cloud droplet generators (Hernandez-Deckers  
593 et al. 2022).

594

595 The convective-grid  $Q_{g+h}$  of the dry case is nearly twice as high as that in the wet case, peaked  
596 around the melting layer (Figs. 8g & 8k), whereas in-thermal  $Q_{g+h}$  shows similar peak values  
597 between the dry and wet cases. As indicated by Fig. 7g, these larger and heavier rimed particles  
598 sediment from thermals and further collision with supercooled liquid must enhance the graupel

599 growth during the sedimentation process, as suggested from aircraft measurements (Blyth and  
600 Latham 1993). Thus, elevated in-thermal  $Q_{g+h}$  in dry-case convection can have further riming  
601 growth after falling out from thermals. This vigorous growth of  $Q_{g+h}$  in dry-case convection  
602 eventually generates vigorous raindrops after the melting process. This could explain why  
603 convective-grid  $Q_r$  in the dry case is larger than that in the wet case (Fig. 8i), opposite from the  
604 result of in-thermal  $Q_r$  (Fig. 8e). Thus, in-thermal  $Q_r$  values are not directly related to total  $Q_r$  in  
605 the convective core (or surface precipitation rate) because of this cold precipitation microphysics  
606 process in deep convection.

607  
608 A second leading question is why the height at the peak value of dry-case in-thermal  $Q_{g+h}$  is more  
609 elevated than the wet-case thermal (Fig. 8g). Fig. 9 shows histograms of thermal properties from  
610 the dry and wet cases. Consistent with the mean vertical profiles (Fig. 8a), more thermals are  
611 initiated below 7 km in the dry case than in the wet case (Z0, Fig. 9d). Thermal radius in the wet  
612 case is also larger than the dry case regardless of shallower boundary layer depths in the wet case  
613 (Fig. 9a), consistent with R in thermal vertical profiles reaching larger sizes at most elevations in  
614 the wet case (Fig. 8b). However, here we see that thermal vertical velocity (W, Fig. 9b), travel  
615 distance (dZ, Fig. 9c), and lifetime (Fig. 9e) in the dry case are all greater than in the wet case.  
616 Thermal entrainment rate is smaller in the dry case than the wet case. These results indicate that  
617 the thermals in the dry-case deep convection can travel longer distances with an extended lifetime  
618 due to a lesser dilution.

619  
620 Interestingly, slightly smaller thermal radii in dry-case convection can have a lower entrainment  
621 rate than in wet-case convection. Hernandez-Deckers and Sherwood (2018) also found that the  
622 variability of thermal radius can only account for 20% of the total variance of thermal dilution rate,  
623 i.e., larger thermal tends to have a lesser dilution rate. This was concluded through similar thermal  
624 tracking analysis from different LESs. Therefore, thermal size is not the sole parameter for  
625 determining dilution rate.

626  
627 Giangrande et al. (2022) suggest that the convective area is smaller in dry-season convection over  
628 this region. Thus, this indicates that stronger low-level buoyancy in dry-season environments can  
629 more narrowly concentrate updraft and low-level thermals in the area, thus creating less diluted

630 environments probably due to the impact of thermal drag (Romps and Charn 2015). This is merely  
631 speculative and requires further investigation to confirm or refute. Takahashi et al. (2022)  
632 investigated cloud-scale entrainment between continental and maritime environments and found a  
633 larger dilution rate in maritime convection than in continental convection. Our results suggest that  
634 this difference in cloud dilution happens from the thermal-process level. These conditions elevate  
635 dry-case thermals and graupel peak concentration toward higher altitudes than the wet-case  
636 convection (Fig. 7f), leading to greater graupel production.

637

638 Finally, time series of thermal properties in the x-z cross-section are constructed for the dry case.  
639 For this, each thermal at its maximum  $w$  value is centered and defined as the time of zero, and  
640 prior (later) steps are represented in negative (positive) time steps. Because of the 1-minute LES  
641 output, the time series from -3 to 3 encompasses 7 minutes of time steps. This averaging process  
642 also weighs upon the magnitude of the thermal mass flux (Hernandez-Deckers et al. 2022); thus,  
643 thermals at larger values in positive and negative time steps tend to have a fewer sampling numbers.  
644 Also, to make the composites, equal-sized thermals are sampled to characterize the mean time  
645 series of thermal properties, avoiding sampling too small thermals, which often has no  
646 supersaturation (Hernandez-Deckers and Sherwood. 2016). This normalization procedure ends up  
647 with the result that maximum  $W$  values do not appear at reference time ( $t=0$ ), but better capture  
648 the evolution of the largest flux-bearing thermals (Fig. 10). We also note that a typical thermal  
649 travel distance is 1.3 km (Fig. 9c) and a minority of dry-case thermals therefore contain either no  
650 ice phase (Fig. 8e-f) or no liquid phase (Fig. 8c-d), but most contain both phases between 3 and 7  
651 km. Note that this flux-weighting is the one way to present the results, while simple non-weighting  
652 averaging can also show similar results.

653

654 In the dry case (Fig. 10), within thermals that experience an extended peak in  $W$  ( $6-11 \text{ m s}^{-1}$ ), the  
655 average supersaturation, cloud, and rain mixing ratio peaks at the earlier steps and decreases  
656 toward the end of the time steps. This indicates that a chunk of condensation heating is the main  
657 initial driver of moist thermal growth. These thermal properties are typically centered around the  
658 thermal core. By contrast,  $Q_{i+s}$  properties are more homogeneous and less concentrated at the core  
659 of thermals, and they tend to increase toward the end of the time series. Especially, the early stages  
660 ( $t=-3, -2, \& -1$ ) indicate thermals are approaching an existing ice layer rather than generating ice

661 around the thermal core. In the later stages ( $t=1, 2, \& 3$ ), the  $Q_{i+s}$  is weakly concentrated toward  
662 the upper thermal cores. This evolution of  $Q_{i+s}$  suggests that thermals are not the main initiator of  
663  $Q_{i+s}$  at the beginning, while  $Q_{i+s}$  is rather entrained into the thermal within the early stages of the  
664 mixed-phase zone, at least using the single-moment bulk microphysics. On the other hand, after  
665 liquid saturation is no longer contributing substantially to  $Q_c$ ,  $Q_{i+s}$  becomes a leading destination  
666 of the overall transfer from vapor to hydrometeor phases within thermals that remain vigorous,  
667 probably due to the Bergeron process (Bergeron 1935). Further research is needed to investigate  
668 the ice nucleation and growth process in greater detail throughout the different stages of thermals'  
669 lifecycle.

670

671 On the other hand,  $Q_{g+h}$  increases toward the peak time of thermals ( $t=0$ ), and starts decreasing  
672 toward the later time steps ( $t=3$ ). The spatial concentration of  $Q_{g+h}$  is also peaked around the  
673 thermal cores, similar to  $W$ ,  $rh$ ,  $Q_c$ , and  $Q_r$ . The increase of  $Q_{g+h}$  coincided with the timing of  
674 thermal entrainment of  $Q_{i+s}$  and a reduction in  $Q_c$  and  $Q_r$  for time steps between  $-3$  and  $0$ . This  
675 suggests that large concentrations of in-thermal  $Q_c$  and  $Q_r$  collide with entrained  $Q_{i+s}$  to enhance  
676 the riming process, generating graupel and hail particles at the thermal core. Note that the 4ICE  
677 scheme only allows wet growth (collecting supercooled liquid) of graupel, while dry growth  
678 (collecting ice and aggregate) of graupel has been suppressed due to unrealistic graupel in  
679 convective anvil (Lang et al. 2014). After the reference time step ( $t=0$ ),  $Q_{g+h}$  decreases, most  
680 likely due to sedimentation exceeding production. As indicated by Fig. 8g & 8k, this spilled  
681 graupel and hail can further grow by colliding with supercooled liquid particles until melting.  
682 Taken together, this analysis also suggests that this vigorous  $Q_{g+h}$ -generation process in the  
683 convective core *does not* occur through the classic parcel-driven convection. Instead, these graupel  
684 and hail generations are most likely driven by sequential interactions of thermal ensembles and  
685 microphysical processes. Note that the time series of the wet case also shows a similar finding but  
686 is biased toward the thermals in the upper atmosphere (not shown here).

687

688 In addition to reference time, we composited thermal properties at different altitude levels (Fig.  
689 11). The method for sampling and compositing is the same as in Fig. 10. However, it characterizes  
690 vertical profiles of thermal composites using altitude references from 2.5km up to 10.5km,  
691 including the mean air temperature. Despite of different reference methods, altitude-reference plots

692 appear to be similar patterns to time-reference plots. Vertical velocity ( $W$ ) increases toward the  
693 peak level at 8.5 km, similar to the mean profile in Fig. 8c. There is strong supersaturation ( $S$ )  
694 between 4.5 km and 6.5 km, which rapidly decreases above 8.5 km.  $Q_c$ ,  $Q_r$ ,  $Q_{i+s}$ , and  $Q_{g+h}$   
695 profiles also resemble thermal-mean profiles in Figs. 8d, 8e, 8f, and 8g, respectively. In thermal  
696 cores,  $Q_c$ ,  $Q_r$ , and  $Q_{g+h}$  are initially concentrated but sediment as thermals ascend. Even  
697 compared with the lifetime composite in Fig. 10,  $Q_{i+s}$  are more stratified horizontally rather than  
698 toward thermal cores, particularly from 3.5 km to 6.5 km, suggesting entrainment of  $Q_{i+s}$  within  
699 thermals at these altitudes. Simultaneously,  $Q_c$  and  $Q_r$  decrease while  $Q_{g+h}$  increases at these  
700 altitudes. Because wet growth (ice collecting supercooled liquid) is the primary graupel growth  
701 process within 4ICE microphysics in the GCE (Lang et al. 2014), the droplet-loaded thermal  
702 penetration toward ice layers appears to be the important graupel/hail generation process within  
703 tropical deep convection.

704

#### 705 **4. Conclusion: Thermal-driven Convection Invigoration Process**

706

707 We have investigated seasonal differences of the measured and simulated  $V_{dop}$  between the dry  
708 and wet seasons to confirm dry-season convective vigor associated with enhanced cold  
709 precipitation (graupel and hail) processes. Tracked thermal properties from the selected case  
710 studies reveal unique updraft microphysics processes in the convective core that explain the dry-  
711 wet contrast in deep convection. To summarize our findings in graupel-hail development  
712 sequences, a thermal-driven process is proposed in the following steps (Fig. 12a).

713

714 1. Where condensation may occur within moist turbulent structures in the lower atmosphere,  
715 local moist thermals may be initiated, which are characterized by dipole vortex rings with  
716 intense vertical velocity, supersaturation, cloud droplets, and raindrops around the thermal  
717 core.

718 2. When moist thermals penetrate the  $0^\circ\text{C}$  isothermal layer and dissipate in the mixed-phase  
719 zone, cloud droplets are detrained and gradually glaciated to form ice-particle layers.

720 3. As additional thermals fill with droplets at the thermal core and penetrate the glaciated  
721 mixed-phase zone, they entrain ice particles and collide with each other, generating graupel  
722 and hail embryos.



723 4. Once graupel and hail particles grow sufficiently large, they start falling out from thermals  
724 and develop further by collecting supercooled droplets and ice particles during  
725 sedimentation.

726  
727 The process of generating ice layers (Step 3) could be the largest source of uncertainty in this study.  
728 To prove the convective vigor process, this study used the simple bulk single-moment  
729 microphysics parameterization (Lang et al. 2014, Tao et al. 2016). This parameterization tends to  
730 convert droplets into ice particles through the saturation adjustment process. Cloud droplets are  
731 glaciated much more quickly when compared to two-moment microphysics (e.g. Matsui et al.  
732 2023). Time series as well as altitude reference composite also shows some ice generation within  
733 the thermal core in later lifecycle stages (~10 km altitude), which may be associated with the  
734 Bergeron process. Yet, ice crystal formation processes remain one of the largest sources of  
735 microphysics uncertainty (Kanji et al. 2017; Korolev and Leisner 2020) and need further  
736 investigation to establish with adequate parameterizations. Furthermore, updrafts passing through  
737 the melting layer containing both large drops and ice crystals (which are identified here as a source  
738 of graupel) have also been pinpointed as a leading source of secondary ice production in oceanic  
739 convection sampled extensively via aircraft (Korolev et al. 2020). Thus, all quantitative  
740 components of the proposed ice-graupel generation process described here remain uncertain and  
741 subject to future investigations via instrumental observations and more detailed numerical  
742 simulations.

743  
744 Nonetheless, building on the ability of existing knowledge and simulations to reproduce some  
745 basic features of observations during GoAmazon, Fig. 12b shows a newly proposed process that  
746 can explain why dry-season convection has more graupel and intense precipitation than wet-season  
747 counterparts in the following steps.

- 748 1. Dry-case (wet-case) convection tends to generate more (less) numbers of droplet-loaded  
749 thermals from the lower atmosphere because of larger potential buoyant energy at a low  
750 level in the dry season.
- 751 2. Once an ice layer is built from initial cumulus thermal ensembles (Fig. 11a), more (less)  
752 numbers of droplet-loaded thermals penetrate ice layers to generate more (less) graupel and  
753 hail embryos in dry-case (wet-case) convection.

754 3. Individual dry-case (wet-case) thermals can rise to higher (lower) elevations via weaker  
755 (stronger) dilution with faster (slower) updraft, elevating in-thermal graupel at higher  
756 (lower) altitudes.

757 4. During sedimentation, graupel in dry-case (wet-case) thermals has a higher (lower) chance  
758 to grow due to the longer (shorter) distance toward the melting level.

759 These new processes are proposed from the “golden” cases from the dry and wet seasons. Further  
760 investigation with more case studies will augment our hypothesis in the future.

761  
762 The “hotter” surface in the dry season must be the physical origin of step 1, similar to L-O contrast  
763 (William and Stanfill, 2002). The dry season typically has clearer skies, less soil moisture, and  
764 stronger surface heating, leading to more turbulent heat flux and energy at the lower troposphere  
765 even during GoAmazon experiment (Biscaro et al., 2021; Ghate and Kollias, 2016). In contrast,  
766 the wet season is characterized by frequent precipitation and increased release of atmospheric  
767 latent heat with the weak surface sensible heat flux caused by wet soil moisture (Rocha et al.,  
768 2004). As a result, the entire troposphere experiences upward motion during the wet season, unlike  
769 its dry season counterpart (Tang et al., 2016).

770  
771 Contrary to the speculation made by William and Stanfill (2002), it has been found that stronger  
772 surface heating and deeper PBL during the dry season do not increase the thermal "size" based on  
773 the classic similarity theory of Morton et al. (1956). Instead, our analysis of simulations indicates  
774 that the numbers and updraft velocity profiles of cumulus thermals become more important,  
775 particularly those initiated in the lower troposphere. Even for similar CAPE, the concentration of  
776 potential buoyancy profiles in the lower troposphere can trigger more vigorous convection. This  
777 is similar to the difference between mid-latitude continental and tropical maritime environments,  
778 where the mid-latitude continental environment tends to have more potential buoyancy in the mid-  
779 to-lower troposphere, leading to continental convective vigor (Matsui et al., 2020). For this, we  
780 need to investigate boundary layer dry thermals and deep-convective moist thermal seamlessly  
781 between various continental and maritime environments.

782  
783 It is also hypothesized that the low-altitude concentrated cumulus thermal trains could additionally  
784 enhance the cold precipitation process by improving the residence time of graupel and hail within

785 the mixed-phase zone if thermal-spilled graupel and hail encounter subsequent new cumulus  
786 thermals. Previous trajectory modeling (Heymsfield 1983) also suggested a similar mechanism for  
787 enhancing graupel and hail residence time and growth by multiple convective cores. Heymsfield  
788 (1983) used the multi-Doppler technique to generate a three-dimensional wind field, but it needed  
789 more spatio-temporal resolution to characterize cumulus thermal. However, a stronger updraft core  
790 mentioned in his study must be cumulus thermals. This investigation further requires a more  
791 complex set of numerical simulations in the future.

792

793 The proposed thermal-driven invigoration process is based solely on thermodynamics and does  
794 not consider aerosols' effect on deep convection, as demonstrated by previous studies over the  
795 Amazon (William et al. 2002, Lin et al. 2006). Our choice of single-moment microphysics does  
796 not consider the variability of background aerosols to initiate cloud droplets. However, this simple  
797 microphysics can generate a fundamental dry-wet contrast characterized by the  $V_{\text{dop}}$  statistics. This  
798 suggests that thermodynamics is the primary factor determining convective vigor, while aerosols  
799 may have a significant but secondary role in invigorating convection (Matsui et al. 2020). Future  
800 studies will require a higher-order moment of microphysics scheme to examine the impact of  
801 aerosols on droplet and primary ice nucleation in thermals to confirm our hypothesis that dry-wet  
802 aerosol contrast plays a secondary role.

803

804 It is well known that severe hailstorms and large hails are more frequently observed over the central  
805 plains of North and South America (Liu and Zipser 2015, Bang and Cecil 2019). The hailstorms  
806 in these regions are often associated with supercells, and mesocyclones play a crucial role in the  
807 growth of very large hail by enhancing the residence time of the hails within the mixed-phase zone  
808 (e.g., Nelson 1983; Ziegler et al. 1983). However, it is not known how a mesocyclone affects  
809 thermal-like or plume-like updraft characteristics (Morrison et al., 2020), though satellites have  
810 captured thermal chain-like periodic overshooting signals at the top of the supercells (Borque et  
811 al. 2020). Thus, further observational and modeling investigations are required for the mid-latitude  
812 regions to determine whether our proposed graupel/hail generation mechanisms can be applied.

813

814 The proposed process for graupel-hail generation and convective vigor is a time-dependent,  
815 sequential, coupled dynamics-microphysics process. Although the traditional plume-based mass

816 flux scheme has been successful in representing the moist convection process in climate models  
817 (e.g., Arakawa and Schubert 1974), our proposed convective microphysics process is not linear  
818 and cannot be adequately represented by the traditional convective mass flux method. To represent  
819 this process, thermal chain concepts with detailed microphysics processes must be introduced in  
820 the parameterization for large-scale models (Morrison et al., 2020). Fine-resolution simulations  
821 produce better continental convective vigor because they can resolve thermal dynamics and  
822 microphysics (Robinson et al., 2011; Matsui et al., 2020). The mean radius of the tracked thermal  
823 in this study, conducted using a 200 m mesh LES, is around 1 km, with a maximum size of around  
824 2 km, which is comparable to the LES study using a 65-m horizontal grid spacing (Hernandez-  
825 Deckers and Sherwood, 2016). However, due to the effective resolution being 5-10 times the actual  
826 grid spacing, cumulus thermals, and graupel-hail generation processes are difficult to resolve for  
827 storm-resolving models and perhaps any coarser Eulerian-type numerical atmospheric models  
828 (Matsui et al., 2016). Conducting LES for regional and global weather and climate models is  
829 impractical in the foreseeable future. Therefore, new types of dynamics-microphysics-coupled  
830 cumulus thermal parameterization should be developed to better represent deep convection for  
831 storm-resolving and coarse-resolution weather and climate models.

832

833 New ground-based Doppler phased array radar (PAR) technology (Kollias et al. 2022b) or multi-  
834 Doppler agile scans (Kollias et al. 2022a) hold promise in observing and characterizing cumulus  
835 thermals. Emerging PAR instruments have started capturing storm motion and microphysical  
836 details at spatial and temporal resolutions akin to those seen in LES output (e.g. Takahashi et al.  
837 2019, Kikuchi et al. 2020). These new observational capabilities are necessary for refining the  
838 dynamics and microphysics in LESs, particularly in elucidating the process behind thermal-driven  
839 convective vigor. Moreover, the advent of vertical motion estimates from high-resolution space-  
840 based radars [EarthCARE, Wehr et al. 2023; Investigation of Convective Updrafts (INCUS),  
841 <https://incus.colostate.edu>; the Atmosphere Observing System (AOS), <https://aos.gsfc.nasa.gov>)  
842 will soon enable the global mapping of convective updrafts. These new satellite radar  
843 measurements will generate a comprehensive global catalog detailing convective vigor and the  
844 speed of intense thermals.

845

846 **Code Availability.** The GCE LES code, G-SDSU simulator code, and Python plotting codes used  
847 in this manuscript are all available in the NCCS Data Portal  
848 ([https://portal.nccs.nasa.gov/datashare/cloudlibrary/PUB\\_DATA/GoAmazon\\_ACP/Code/](https://portal.nccs.nasa.gov/datashare/cloudlibrary/PUB_DATA/GoAmazon_ACP/Code/)).

849  
850 **Data Availability.** The RWP measurements and VARNAL LSF data were available from the  
851 Atmospheric Radiation Measurement (ARM) ARM Data Discovery  
852 (<https://adc.arm.gov/discovery/#/>). These data were obtained from the ARM Mobile Facility  
853 (AMF) at Manacapuru, Amazonas, Brazil, funded by A. U.S. Department of Energy (DOE) Office  
854 of Science User Facility managed by the Biological and Environmental Research program. The  
855 analysis data used in this manuscript is also available in the NCCS Data Portal  
856 ([https://portal.nccs.nasa.gov/datashare/cloudlibrary/PUB\\_DATA/GoAmazon\\_ACP/Data/](https://portal.nccs.nasa.gov/datashare/cloudlibrary/PUB_DATA/GoAmazon_ACP/Data/))

857  
858 **Author contribution.** T. Matsui designed and performed the GCE LESs, the  $V_{dop}$  forward  
859 simulation, and the thermal tracking. D. Hernandez-Deckers developed the thermal tracking and  
860 analysis code for the GCE LESs and prepared the  $V_{dop}$  figures for the thermal analysis. S.  
861 Giangrande and T. Biscaro prepared RWP  $V_{dop}$  analysis. T. Matsui prepared the manuscript with  
862 contributions from all co-authors.

863  
864 **Competing interests.** At least one of the (co-)authors is a member of the editorial board of  
865 Atmospheric Chemistry and Physics.

866  
867 **Acknowledgments.** This project is funded by the NASA CloudSat and CALIPSO Science Team  
868 (CCST) program (program manager: Dr. David Considine, grant number: 80NSSC21K1135). The  
869 development of GCE is funded by the NASA GSFC Strategic Science resources (Associate  
870 Director for Institutional Planning and Operation: Dr. Karen Mohr). We also thank the NASA  
871 Advanced Supercomputing (NAS) Division and Center for Climate Simulation (NCCS) (Project  
872 Manager T. Lee at NASA HQ) for providing the computational resources to conduct the GCE and  
873 G-SDSU simulations, thermal tracking analysis, and stored model outputs. The authors thank an  
874 anonymous reviewer for improving the manuscript.

875

876 **References**

- 877 Arakawa, A. and Schubert, W. H. (1974): Interaction of a cumulus cloud ensemble with the  
878 large-scale environment, Part I, *J. Atmos. Sci.*, 31, 674–701.
- 879 Bang, S. D., and D. J. Cecil, 2019: Constructing a Multifrequency Passive Microwave Hail  
880 Retrieval and Climatology in the GPM Domain. *J. Appl. Meteor. Climatol.*, 58, 1889–  
881 1904, <https://doi.org/10.1175/JAMC-D-19-0042.1>.
- 882 Biscaro, T. S., Machado, L. A. T., Giangrande, S. E., and Jensen, M. P. (2021): What drives  
883 daily precipitation over the central Amazon? Differences observed between wet and dry  
884 seasons, *Atmos. Chem. Phys.*, 21, 6735–6754, <https://doi.org/10.5194/acp-21-6735-2021>.
- 885 Blyth, A. M., S. G. Lasher-Trapp, and W. A. Cooper (2005): A study of thermals in cumulus  
886 clouds, *Quarterly Journal of the Royal Meteorological Society*, 131, 1171–1190,  
887 <https://doi.org/10.1256/qj.03.180>.
- 888 Borque, P., Vidal, L., Rugna, M., Lang, T. J., Nicora, M. G., & Nesbitt, S. W. (2020). Distinctive  
889 Signals in 1-min Observations of Overshooting Tops and Lightning Activity in a Severe  
890 Supercell Thunderstorm. *Journal of Geophysical Research: Atmospheres*, 125(20),  
891 e2020JD032856. <https://doi.org/10.1029/2020JD032856>
- 892 Chou, M.-D. and Suarez, M. J. (1999): A solar radiation parameterization for atmospheric  
893 studies, NASA Tech. Rep. NASA/TM-1999-10460, vol 15, p 38,  
894 <https://ntrs.nasa.gov/archive/nasa/casi.ntrs.nasa.gov/19990060930.pdf>.
- 895 Chou, M.-D. and Suarez, M. J. (2001): A thermal infrared radiation parameterization for  
896 atmospheric studies, NASA/TM-2001-104606, vol 19, p 55,  
897 <https://ntrs.nasa.gov/archive/nasa/casi.ntrs.nasa.gov/20010072848.pdf>.

898 Dolan, B., B. Fuchs, S. A. Rutledge, E. A. Barnes, and E. J. Thompson (2018): Primary Modes  
899 of Global Drop Size Distributions, *J. Atmos. Sci.*, 75, 1453–1476,  
900 <https://doi.org/10.1175/JAS-D-17-0242.1>.

901 Emanuel, K. A., David Neelin, J., and Bretherton, C. S. (1994): On large-scale circulations in  
902 convecting atmospheres, *Q. J. R. Meteorol. Soc.*, 120, 1111–1143,  
903 <https://doi.org/10.1002/qj.49712051902>.

904 Ghate, V. P. and Kollias, P. (2016): On the Controls of Daytime Precipitation in the Amazonian  
905 Dry Season, *J. Hydrometeorol.*, 17, 3079–3097, [https://doi.org/10.1175/JHM-D-16-](https://doi.org/10.1175/JHM-D-16-0101.1)  
906 [0101.1](https://doi.org/10.1175/JHM-D-16-0101.1).

907 Giangrande, S. E., Biscaro, T. S., and Peters, J. M. (2023): Seasonal controls on isolated  
908 convective storm drafts, precipitation intensity, and life cycle as observed during  
909 GoAmazon2014/5, *Atmospheric Chemistry and Physics*, 23, 5297–5316,  
910 <https://doi.org/10.5194/acp-23-5297-2023>.

911 Giangrande, S. E., Feng, Z., Jensen, M. P., Comstock, J. M., Johnson, K. L., Toto, T., Wang, M.,  
912 Burleyson, C., Bharadwaj, N., Mei, F., Machado, L. A. T., Manzi, A. O., Xie, S., Tang,  
913 S., Silva Dias, M. A. F., de Souza, R. A. F., Schumacher, C., and Martin, S. T. (2017):  
914 Cloud characteristics, thermodynamic controls and radiative impacts during the  
915 Observations and Modeling of the Green Ocean Amazon (GoAmazon2014/5)  
916 experiment, *Atmospheric Chemistry and Physics*, 17, 14519–14541,  
917 <https://doi.org/10.5194/acp-17-14519-2017>.

918 Giangrande, S. E., Toto, T., Jensen, M. P., Bartholomew, M. J., Feng, Z., Protat, A., Williams, C.  
919 R., Schumacher, C., and Machado, L. (2016): Convective cloud vertical velocity and  
920 mass-flux characteristics from radar wind profiler observations during GoAmazon2014/5,

921 Journal of Geophysical Research: Atmospheres, 121, 12,891–12,913,  
922 <https://doi.org/10.1002/2016JD025303>.

923 Giangrande, S. E., Wang, D., and Mechem, D. B. (2020): Cloud regimes over the Amazon  
924 Basin: perspectives from the GoAmazon2014/5 campaign, Atmospheric Chemistry and  
925 Physics, 20, 7489–7507, <https://doi.org/10.5194/acp-20-7489-2020>.

926 Giangrande, S. E., E. P. Luke, and P. Kollias (2012): Characterization of Vertical Velocity and  
927 Drop Size Distribution Parameters in Widespread Precipitation at ARM Facilities,  
928 Journal of Applied Meteorology and Climatology, 51, 380–391,  
929 <https://doi.org/10.1175/JAMC-D-10-05000.1>.

930 Giangrande, S. E., S. Collis, J. Straka, A. Protat, C. Williams, and S. Krueger (2013): A  
931 Summary of Convective-Core Vertical Velocity Properties Using ARM UHF Wind  
932 Profilers in Oklahoma, Journal of Applied Meteorology and Climatology, 52, 2278–2295,  
933 <https://doi.org/10.1175/JAMC-D-12-0185.1>.

934 Grabowski, W. W. & Petch, Jon (2009): Deep Convective Clouds. Clouds in the Perturbed  
935 Climate System: Their Relationship to Energy Balance. 2. 197-215,  
936 <https://doi.org/10.7551/mitpress/9780262012874.003.0009>.

937 Gu, J.-F., Plant, R. S., Holloway, C. E., and Muetzelfeldt, M. R. (2020): Pressure drag for  
938 shallow cumulus clouds: From thermals to the cloud ensemble, Geophysical Research  
939 Letters, 47, e2020GL090460, <https://doi.org/10.1029/2020GL090460>.

940 Hartmann, D. L. (2016): Global Physical Climatology, 2nd ed., Academic Press, Cambridge,  
941 UK, ISBN: 978-0-12-328531-7, DOI: <https://doi.org/10.1016/C2009-0-00030-0>.



942 Hernandez-Deckers, D. and Sherwood, S. C. (2016): A Numerical Investigation of Cumulus  
943 Thermals, *Journal of the Atmospheric Sciences*, 73, 4117–4136, DOI: 10.1175/JAS-D-  
944 15-0385.1.

945 Hernandez-Deckers, D. and Sherwood, S. C. (2018): On the Role of Entrainment in the Fate of  
946 Cumulus Thermals, *Journal of the Atmospheric Sciences*, 75, 3911–3924, DOI:  
947 10.1175/JAS-D-18-0077.1.

948 Hernandez-Deckers, D., Matsui, T., and Fridlind, A. M. (2022): Updraft dynamics and  
949 microphysics: On the added value of the cumulus thermal reference frame in simulations  
950 of aerosol-deep convection interactions, *Atmospheric Chemistry and Physics*, 22(2), 711–  
951 724, DOI: 10.5194/acp-22-711-2022.

952 Heymsfield, A. J. (1983): Case Study of a Halistorm in Colorado. Part IV: Graupel and Hail  
953 Growth Mechanisms Deduced through Particle Trajectory Calculations, *J. Atmos. Sci.*,  
954 40, 1482–1509, [https://doi.org/10.1175/1520-0469\(1983\)040<1482:CSOAH1>2.0.CO;2](https://doi.org/10.1175/1520-0469(1983)040<1482:CSOAH1>2.0.CO;2).

955 Holland, G. J., John, L., McBride, R. K., Smith, D. J., Jasper, D., and Keenan, T. D. (1986): The  
956 BMRC Australian Monsoon Experiment: AMEX, *Bulletin of the American*  
957 *Meteorological Society*, 67(12), 1466-1472, doi: 10.1175/1520-  
958 0477(1986)067<1466:TBAMEA>2.0.CO;2.

959 Iguchi, T., Matsui, T., Tao, W., Khain, A., Phillips, V., Kidd, C., L'Ecuyer, T., Braun, S., and  
960 Hou, A. (2014): WRF-SBM simulations of melting layer structure in mixed-phase  
961 precipitation events observed during LPVEx, *J. Appl. Meteor. Climatol.*, 53, 2710-2731,  
962 doi:10.1175/JAMC-D-13-0334.1.

963 Jeyaratnam, J., Luo, Z. J., Giangrande, S. E., Wang, D., & Masunaga, H. (2021): A satellite-  
964 based estimate of convective vertical velocity and convective mass flux: Global survey

965 and comparison with radar wind profiler observations, *Geophysical Research Letters*, 48,  
966 e2020GL090675, <https://doi.org/10.1029/2020GL090675>.

967 Kanji, Z. A., Ladino, L. A., Wex, H., Boose, Y., Burkert-Kohn, M., Cziczo, D. J., & Krämer, M.  
968 (2017): Overview of Ice Nucleating Particles, *Meteorological Monographs*, 58, 1.1–1.33,  
969 DOI: 10.1175/AMSMONOGRAPHS-D-16-0006.1.

970 Keenan, T. D. and Carbone, R. E. (1992): A Preliminary Morphology of Precipitation Systems In  
971 Tropical Northern Australia, *Q.J.R. Meteorol. Soc.*, 118: 283-326,  
972 <https://doi.org/10.1002/qj.49711850406>.

973 Kikuchi, H. et al. (2020): Initial observations for precipitation cores with X-band dual polarized  
974 phased array weather radar, *IEEE Transactions on Geoscience and Remote Sensing*,  
975 58(5), 3657-3666, <http://doi.org/10.1109/TGRS.2019.2959628>.

976 Kollias, P., Luke, E. P., Tuftedal, K., Dubois, M., & Knapp, E. J. (2022): Agile Weather  
977 Observations using a Dual-Polarization X-band Phased Array Radar, 2022 IEEE Radar  
978 Conference (RadarConf22), New York City, NY, USA, pp. 1-6, doi:  
979 10.1109/RadarConf2248738.2022.9764308.

980 Kollias, P., Luke, E., Tuftedal, K., Dubois, M., & Knapp, E. J. (2022): Agile weather  
981 observations using a dual-polarization X-band phased array radar, 2022 IEEE Radar  
982 Conf., New York, NY, IEEE, 1–6,  
983 <https://doi.org/10.1109/RadarConf2248738.2022.9764308>.

984 Kollias, P., & Coauthors (2022): Science Applications of Phased Array Radars, *Bull. Amer.*  
985 *Meteor. Soc.*, 103, E2370–E2390, <https://doi.org/10.1175/BAMS-D-21-0173.1>.

986 Korolev, A., Heckman, I., Wolde, M., Ackerman, A. S., Fridlind, A. M., Ladino, L. A., Lawson,  
987 R. P., Milbrandt, J., and Williams, E. (2020): A new look at the environmental conditions

988 favorable to secondary ice production, *Atmos. Chem. Phys.*, 20, 1391–1429,  
989 <https://doi.org/10.5194/acp-20-1391-2020>.

990 Korolev, A. and Leisner, T. (2020): Review of experimental studies of secondary ice production,  
991 *Atmos. Chem. Phys.*, 20, 11767–11797, <https://doi.org/10.5194/acp-20-11767-2020>.

992 Lang, S. E., Tao, W.-K., Chern, J.-D., Wu, D., & Li, X. (2014): Benefits of a fourth ice class in  
993 the simulated radar reflectivities of convective systems using a bulk microphysics  
994 scheme, *J. Atmos. Sci.*, 71, 3583–3612, <https://doi.org/10.1175/JAS-D-13-0330.1>.

995 Lin, J. C., Matsui, T., Pielke Sr., R. A., & Kummerow, C. (2006): Effects of biomass burning-  
996 derived aerosols on precipitation and clouds in the Amazon Basin: A satellite-based  
997 empirical study, *Journal of Geophysical Research*, 111, D19204,  
998 doi:10.1029/2005JD006884.

999 Liu, C., & Zipser, E. J. (2015). The global distribution of largest, deepest, and most intense  
1000 precipitation systems. *Geophysical Research Letters*, 42(9), 3591-3595.  
1001 <https://doi.org/10.1002/2015GL063776>

1002 Lucas, C., Zipser, E. J., & Lemone, M. A. (1994): Vertical velocity in oceanic convection off  
1003 tropical Australia, *J. Atmos. Sci.*, 51, 3183–3193, doi:10.1175/1520-  
1004 0469(1994)051,3183: VVIOCO.2.0.CO;2.

1005 Martin, S. T., & Coauthors (2017): The Green Ocean Amazon Experiment (GoAmazon2014/5)  
1006 Observes Pollution Affecting Gases, Aerosols, Clouds, and Rainfall over the Rain Forest,  
1007 *Bulletin of the American Meteorological Society*, 98, 981–997, DOI: 10.1175/BAMS-D-  
1008 15-00221.1.

1009 Matsui, T., & Mocko, D. M. (2014): Transpiration and Physical Evaporation: Regional and  
1010 Seasonal Variability Over the Conterminous United States, In *Encyclopedia of Natural*

1011 Resources, 1st Ed.; Wang, Y. Q., Ed.; Taylor & Francis Group: New York. 1086pp,  
1012 ISBN 9781439852583 - CAT# K12418.

1013 Matsui, T., & Coauthors (2014a): Current and Future Perspectives of Aerosol Research at NASA  
1014 Goddard Space Flight Center, BAMS Meeting Summary 95, ES203–ES207, doi:  
1015 <http://dx.doi.org/10.1175/BAMS-D-13-00153.1>.

1016 Matsui, T., & Coauthors (2014b): Introducing multisensor satellite radiance-based evaluation for  
1017 regional Earth System modeling, *Journal of Geophysical Research*, 119, 8450–8475,  
1018 doi:10.1002/2013JD021424.

1019 Matsui, T., & Coauthors (2016): On the land-ocean contrast of tropical convection and  
1020 microphysics statistics derived from TRMM satellite signals and global storm-resolving  
1021 models, *Journal of Hydrometeorology*, 17, 1425-1445, doi:10.1175/JHM-D-15-0111.1.

1022 Matsui, T., & Coauthors (2018): Impact of Radiation Frequency, Precipitation Radiative Forcing,  
1023 and Radiation Column Aggregation on Convection-Permitting West African Monsoon  
1024 Simulations, *Climate Dynamics*, 1-21, <https://doi.org/10.1007/s00382-018-4187-2>.

1025 Matsui, T., & Coauthors (2020): Polarimetric Radar Characteristics of Simulated and Observed  
1026 Intense Convective Cores for a Midlatitude Continental and Tropical Maritime  
1027 Environment, *J. Hydrometeor.*, 21, 501–517, <https://doi.org/10.1175/JHM-D-19-0185.1>.

1028 Matsui, T., & Coauthors (2023): Systematic validation of ensemble cloud-process simulations  
1029 using polarimetric radar observations and simulator over the NASA Wallops Flight  
1030 Facility, *Journal of Geophysical Research: Atmospheres*, 128, e2022JD038134,  
1031 <https://doi.org/10.1029/2022JD038134>.

1032 Morrison, H., Peters, J. M., Varble, A. C., Hannah, W. M., & Giangrande, S. E. (2020). Thermal  
1033 Chains and Entrainment in Cumulus Updrafts. Part I: Theoretical Description. *Journal of*  
1034 *the Atmospheric Sciences*, 77, 3637–3660. [DOI: 10.1175/JAS-D-19-0243.1]

1035 Morrison, H., Jeevanjee, N., Lecoanet, D., & Peters, J. M. (2023). What controls the entrainment  
1036 rate of dry buoyant thermals with varying initial aspect ratio?. *Journal of the Atmospheric*  
1037 *Sciences*, [DOI: 10.1175/JAS-D-23-0063.1], in press.

1038 Morton, B. R., Taylor, G. I., & Turner, J. S. (1956): Turbulent gravitational convection from  
1039 maintained and instantaneous sources. *Proc. Roy. Soc. London*, 234A, 1–23,  
1040 <https://doi.org/10.1098/RSPA.1956.0011>.

1041 Nelson, S. P., 1983: The influence of storm flow structure on hail growth. *J. Atmos. Sci.*, 40,  
1042 1965–1983, [https://doi.org/10.1175/1520-0469\(1983\)040<1965:TIOSFS>2.0.CO;2](https://doi.org/10.1175/1520-0469(1983)040<1965:TIOSFS>2.0.CO;2).

1043 Öktem, R., Romps, D. M., & Varble, A. C. (2023). No Warm-Phase Invigoration of Convection  
1044 Detected during GoAmazon. *Journal of the Atmospheric Sciences*, 80, 2345–2364. [DOI:  
1045 10.1175/JAS-D-22-0241.1]

1046 Peters, J. M., Morrison, H., Varble, A. C., Hannah, W. M., & Giangrande, S. E. (2020). Thermal  
1047 Chains and Entrainment in Cumulus Updrafts. Part II: Analysis of Idealized Simulations.  
1048 *Journal of the Atmospheric Sciences*, 77, 3661–3681. [DOI: 10.1175/JAS-D-19-0244.1]

1049 Pielke, R. A. (2001). Influence of the spatial distribution of vegetation and soils on the prediction  
1050 of cumulus convective rainfall. *Rev. Geophys.*, 39, 151–177,  
1051 doi:10.1029/1999RG000072.

1052 Pope, M., Jakob, C., & Reeder, M. J. (2009). Regimes of the North Australian Wet Season.  
1053 *Journal of Climate*, 22, 6699–6715. [DOI: 10.1175/2009JCLI3057.1]

1054 Prein, A. F., Ge, M., Valle, A. R., Wang, D., & Giangrande, S. E. (2022). Towards a unified  
1055 setup to simulate mid-latitude and tropical mesoscale convective systems at kilometer-  
1056 scales. *Earth and Space Science*, 9. [DOI: 10.1029/2022EA002295]

1057 Ramos-Valle, A. N., Prein, A. F., Ge, M., Wang, D., & Giangrande, S. E. (2023). Grid spacing  
1058 sensitivities of simulated mid-latitude and tropical mesoscale convective systems in the  
1059 convective gray zone. *Journal of Geophysical Research: Atmospheres*, 128. [DOI:  
1060 10.1029/2022JD037043]

1061 Robinson, F., Sherwood, S., Gerstle, D., Liu, C., & Kirshbaum, D. (2011). Exploring the land-  
1062 ocean contrast in convective vigor using islands. *J. Atmos. Sci.*, 68, 602–618,  
1063 <https://doi.org/10.1175/2010JAS3558.1>.

1064 Rocha, H. R., Goulden, M., Miller, S. D., Menton, M. C., Pinto, L. D. V. O., Freitas, H. C., &  
1065 Figueira, A. M. S. (2004). Seasonality of water and heat fluxes over a tropical forest in  
1066 eastern Amazonia. *Ecol. Appl.*, 14, 22–32.

1067 Romps, D. M., & Charn, A. B. (2015). Sticky Thermals: Evidence for a Dominant Balance  
1068 between Buoyancy and Drag in Cloud Updrafts. *J. Atmos. Sci.*, 72, 2890–2901,  
1069 <https://doi.org/10.1175/JAS-D-15-0042.1>.

1070 Sherwood, S. C., Hernández-Deckers, D., Colin, M., & Robinson, F. (2013). Slippery Thermals  
1071 and the Cumulus Entrainment Paradox. *Journal of the Atmospheric Sciences*, 70, 2426–  
1072 2442, [DOI: 10.1175/JAS-D-12-0220.1]

1073 Steiner, M., Houze Jr., R. A., & Yuter, S. E. (1995). Climatological characterization of three-  
1074 dimensional storm structure from operational radar and rain gauge data. *Journal of*  
1075 *Applied Meteorology*, 34, 1978–2007.

1076 Stephens, G. L., Vane, D. G., Boain, R. J., Mace, G. G., Sassen, K., Wang, Z., ... CloudSat  
1077 Science Team (2002). The CloudSat mission and the A-Train: A new dimension of  
1078 space-based observations of clouds and precipitation. *Bull. Amer. Meteorol. Soc.*, 83,  
1079 1771-1790, doi:10.1175/BAMS-83-12-1771.

1080 Stolz, D. C., Rutledge, S. A., & Pierce, J. R. (2015). Simultaneous influences of thermodynamics  
1081 and aerosols on deep convection and lightning in the tropics. *J. Geophys. Res. Atmos.*,  
1082 120, 6207–6231, <https://doi.org/10.1002/2014JD023033>.

1083 Sullivan, S. C., Voigt, A. (2021). Ice microphysical processes exert a strong control on the  
1084 simulated radiative energy budget in the tropics. *Commun Earth Environ* 2, 137,  
1085 <https://doi.org/10.1038/s43247-021-00206-7>

1086 Takahashi, H., Luo, Z. J., & Stephens, G. L. (2017). Level of neutral buoyancy, deep convective  
1087 outflow, and convective core: New perspectives based on 5 years of CloudSat data.  
1088 *Journal of Geophysical Research: Atmospheres*, 122(5), 2958-2969.

1089 Takahashi, H., Luo, Z. J., & Stephens, G. L. (2021). Revisiting the entrainment relationship of  
1090 convective plumes: A perspective from global observations. *Geophys. Res. Lett.*,  
1091 <https://doi.org/10.1029/2020GL092349>

1092 Takahashi, N., et al. (2019). Development of multi-parameter phased array weather radar (MP-  
1093 PAWR) and early detection of torrential rainfall and tornado risk. *Journal of Disaster*  
1094 *Research*, 14(2), 235-247, <http://doi.org/10.20965/jdr.2019.p0235>

1095 Tang, S., Xie, S., Zhang, Y., Zhang, M., Schumacher, C., Upton, H., Jensen, M. P., Johnson, K.  
1096 L., Wang, M., Ahlgrimm, M., Feng, Z., Minnis, P., and Thieman, M. (2016). Large-scale  
1097 vertical velocity, diabatic heating and drying profiles associated with seasonal and diurnal

1098 variations of convective systems observed in the GoAmazon2014/5 experiment. *Atmos.*  
1099 *Chem. Phys.*, 16, 14249–14264, <https://doi.org/10.5194/acp-16-14249-2016>.

1100 Tao, W.-K., Lang, S., Zeng, X., Li, X., Matsui, T., Mohr, K., Posselt, D., Chern, J., Peters-  
1101 Lidard, C., Norris, P. M., Kang, I.-S., Choi, I., Hou, A., Lau, K.-M., and Yang, Y.-M.  
1102 (2014). The Goddard Cumulus Ensemble model (GCE): improvements and applications  
1103 for studying precipitation processes. *Atmospheric Research*, 143, 392-424. doi:  
1104 <http://dx.doi.org/10.1016/j.atmosres.2014.03.005>.

1105 Tao, W.-K., Wu, D., Lang, S., Chern, J.-D., Peters-Lidard, C., Fridlind, A., and Matsui, T.  
1106 (2016). High-resolution NU-WRF simulations of a deep convective-precipitation system  
1107 during MC3E: Further improvements and comparisons between Goddard microphysics  
1108 schemes and observations. *J. Geophys. Res. Atmos.*, 121, 1278–1305,  
1109 <https://doi.org/10.1002/2015JD023986>.

1110 Tao, K., Iguchi, T., Lang, S., Li, X., Mohr, K., Matsui, T., & Braun, S. (2022). Relating Vertical  
1111 Velocity and Cloud/Precipitation Properties: A Numerical Cloud Ensemble Modeling  
1112 Study of Tropical Convection. *Journal of Advances in Modeling Earth*  
1113 *Systems*, 14(9), e2021MS002677. <https://doi.org/10.1029/2021MS002677>

1114 Tokay, A., and Short, D. A. (1996). Evidence from Tropical Raindrop Spectra of the Origin of  
1115 Rain from Stratiform versus Convective Clouds. *Journal of Applied Meteorology and*  
1116 *Climatology*, 35, 355–371. [DOI: 10.1175/1520-  
1117 0450(1996)035<0355:EFTRSO>2.0.CO;2]

1118 Wang, D., Giangrande, S. E., Bartholomew, M. J., Hardin, J., Feng, Z., Thalman, R., and  
1119 Machado, L. A. T. (2018). The Green Ocean: precipitation insights from the



1120 GoAmazon2014/5 experiment. *Atmospheric Chemistry and Physics*, 18, 9121–9145.  
1121 [DOI: 10.5194/acp-18-9121-2018]

1122 Wang, D., Giangrande, S. E., Schiro, K., Jensen, M. P., & Houze, R. A. (2019). The  
1123 characteristics of tropical and midlatitude mesoscale convective systems as revealed by  
1124 radar wind profilers. *Journal of Geophysical Research: Atmospheres*, 124, 4601–4619.  
1125 [DOI: 10.1029/2018JD030087]

1126 Wehr, T., Kubota, T., Tzeremes, G., Wallace, K., Nakatsuka, H., Ohno, Y., Koopman, R., Rusli,  
1127 S., Kikuchi, M., Eisinger, M., Tanaka, T., Taga, M., Deghaye, P., Tomita, E., and  
1128 Bernaerts, D. (2023). The EarthCARE mission – science and system overview. *Atmos.*  
1129 *Meas. Tech.*, 16, 3581–3608, <https://doi.org/10.5194/amt-16-3581-2023>.

1130 Williams, E., and Stanfill, S. (2002). The physical origin of the land–ocean contrast in lightning  
1131 activity. *C. R. Phys.*, 3, 1277–1292, doi:10.1016/S1631-0705(02)01407-X.

1132 Williams, E., Chan, T., and Boccippio, D. (2004). Islands as miniature continents: Another look  
1133 at the land–ocean lightning contrast. *J. Geophys. Res.*, 109, D16206,  
1134 doi:10.1029/2003JD003833.

1135 Williams, E., Mushtak, V., Rosenfeld, D., Goodman, S., and Boccippio, D. (2005).  
1136 Thermodynamic conditions favorable to superlative thunderstorm updraft, mixed phase  
1137 microphysics and lightning flash rate. *Atmos. Res.*, 76, 288–306,  
1138 doi:10.1016/j.atmosres.2004.11.009.

1139 Williams, C. R., Barrio, J., Johnston, P. E., Muradyan, P., and Giangrande, S. E. (2023).  
1140 Calibrating radar wind profiler reflectivity factor using surface disdrometer observations.  
1141 *Atmospheric Measurement Techniques*, 16, 2381–2398. [DOI: 10.5194/amt-16-2381-  
1142 2023]

1143 Wu, J., Del Genio, A. D., Yao, M.-S., and Wolf, A. B. (2009). WRF and GISS SCM simulations  
1144 of convective updraft properties during TWP-ICE. *Journal of Geophysical Research*, 114,  
1145 D04206. [DOI: 10.1029/2008JD010851]

1146 Xie, S., Cederwall, R. T., and Zhang, M. (2004). Developing long-term single-column  
1147 model/cloud system-resolving model forcing data using numerical weather prediction  
1148 products constrained by surface and top of the atmosphere observations. *J. Geophys.*  
1149 *Res.*, 109, D01104, doi:10.1029/2003JD004045.

1150 Xu, X., Sun, C., Lu, C., Liu, Y., Zhang, G. J., and Chen, Q. (2021). Factors affecting entrainment  
1151 rate in deep convective clouds and parameterizations. *Journal of Geophysical Research:*  
1152 *Atmospheres*, 126, e2021JD034881. [DOI: 10.1029/2021JD034881]

1153 Yanai, M., Esbensen, S., and Chu, J. (1973). Determination of Bulk Properties of Tropical Cloud  
1154 Clusters from Large-Scale Heat and Moisture Budgets. *J. Atmos. Sci.*, 30, 611–627,  
1155 [https://doi.org/10.1175/1520-0469\(1973\)030<0611:DOBPOT>2.0.CO;2](https://doi.org/10.1175/1520-0469(1973)030<0611:DOBPOT>2.0.CO;2).

1156 Yuter, S. E., and Houze Jr., R. A. (1995). Three-dimensional kinematic and microphysical  
1157 evolution of Florida cumulonimbus. Part II: Frequency distribution of vertical velocity,  
1158 reflectivity, and differential reflectivity. *Monthly Weather Review*, 123, 1941–1963.

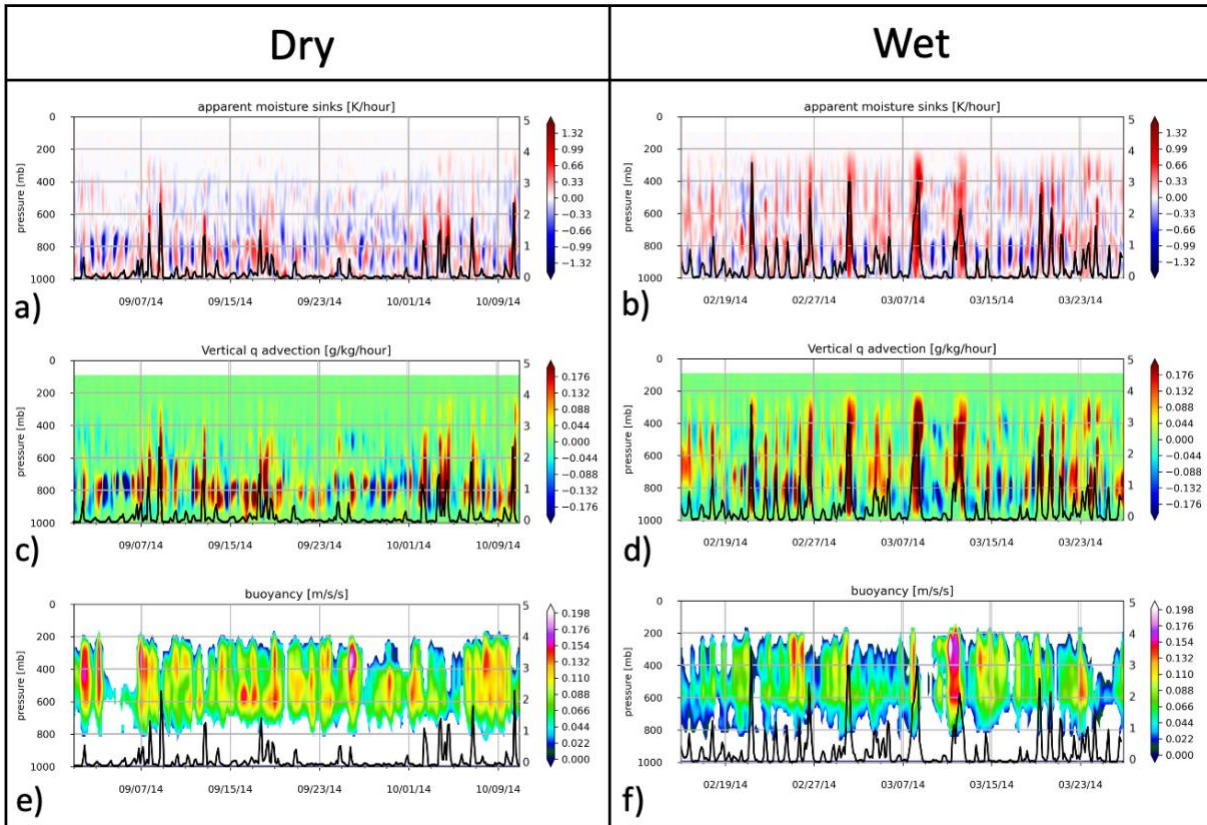
1159 Zipser, E. J., Liu, C., Cecil, D. J., Nesbitt, S. W., and Yorty, D. P. (2006). Where are the most  
1160 intense thunderstorms on Earth? *Bull. Amer. Meteor. Soc.*, 87, 1057–1071,  
1161 doi:10.1175/BAMS-87-8-1057.

1162 Zhang, M., and Lin, J. (1997). Constrained variational analysis of sounding data based on  
1163 column-integrated budgets of mass, heat, moisture, and momentum: Approach and  
1164 application to ARM measurements. *J. Atmos. Sci.*, 54(11), 1503–1524,  
1165 doi:10.1175/1520-0469(1997)054<1503:CVAOSD>2.0.CO;2.

1166 Zhang, M., Lin, J., Cederwall, R. T., Yio, J. J., and Xie, S. C. (2001). Objective analysis of ARM  
1167 IOP data: Method and sensitivity. *Mon. Weather Rev.*, 129(2), 295–311,  
1168 doi:10.1175/1520-0493(2001)129<0295:OAOAID>2.0.CO;2.

1169 Ziegler, C. L., P. S. Ray, and N. C. Knight, 1983: Hail growth in an Oklahoma multicell storm. *J.*  
1170 *Atmos. Sci.*, 40, 1768–1791, [https://doi.org/10.1175/1520-](https://doi.org/10.1175/1520-0469(1983)040<1768:HGIAOM>2.0.CO;2)  
1171 [0469\(1983\)040<1768:HGIAOM>2.0.CO;2](https://doi.org/10.1175/1520-0469(1983)040<1768:HGIAOM>2.0.CO;2).

1172  
1173  
1174



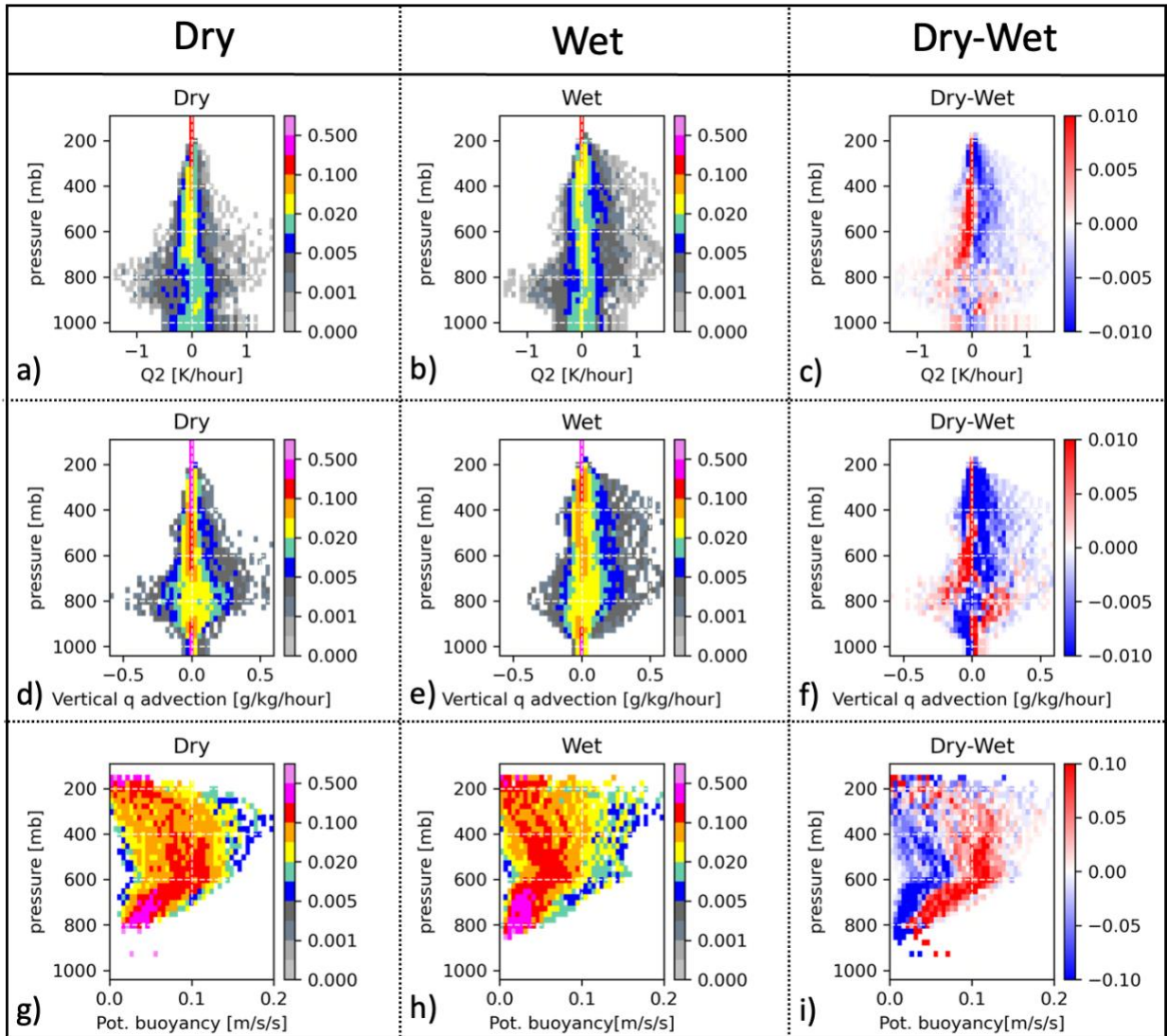
1176

1177 Figure 1. Time series of VARNAL large-scale forcing profiles between wet and dry periods: (a-b)  
 1178 apparent moisture sink ( $Q_2$ ), (c-d) vertical moisture advection, (e-f) potential buoyancy. The black  
 1179 solid lines on the secondary y-axis represent the surface precipitation rate.

1180

1181

1182



1183

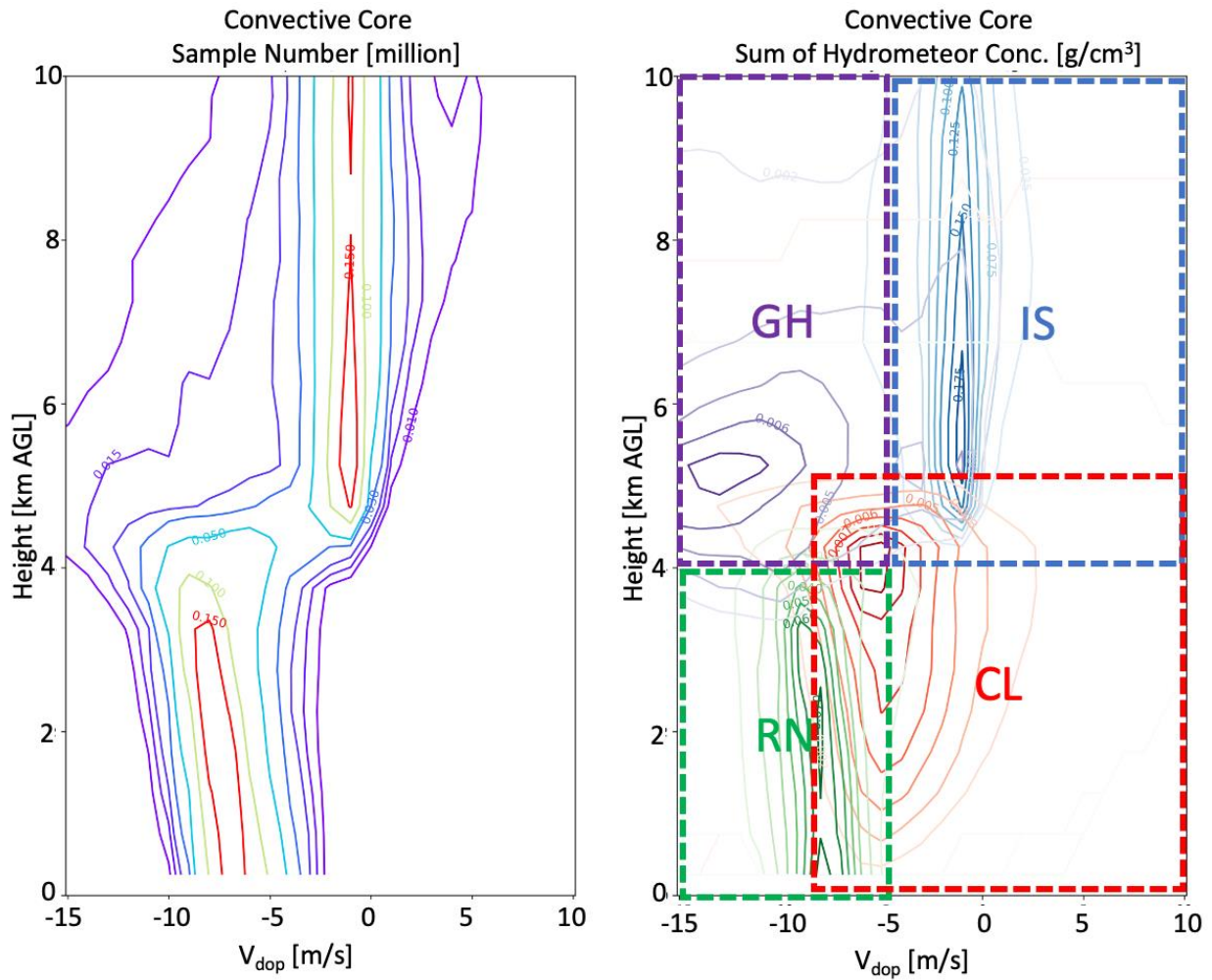
1184 Figure 2. Contoured Frequency of Altitude Diagram (CFADs) of (a-c) apparent moisture sink (Q2),  
 1185 (d-f) vertical moisture (q) advection, (g-i) potential buoyancy integrated over dry and wet periods,  
 1186 as well as dry-wet differences.

1187

1188

1189

1190



1191

1192 Figure 3. (a) Cumulative  $V_{dop}$  sample numbers from LESs during dry and wet periods, presented  
1193 as CFADs for each  $V_{dop}$  bin and altitude. (b) the cumulative hydrometeor mass concentrations  
1194 from each  $V_{dop}$ -altitude bin. Red contours represent “cloud (CL)”, green contours represent “rain  
1195 (RN)” blue contours represent “ice and snow (IS)”, and purple contours represent “graupel and  
1196 hail (GH)”.

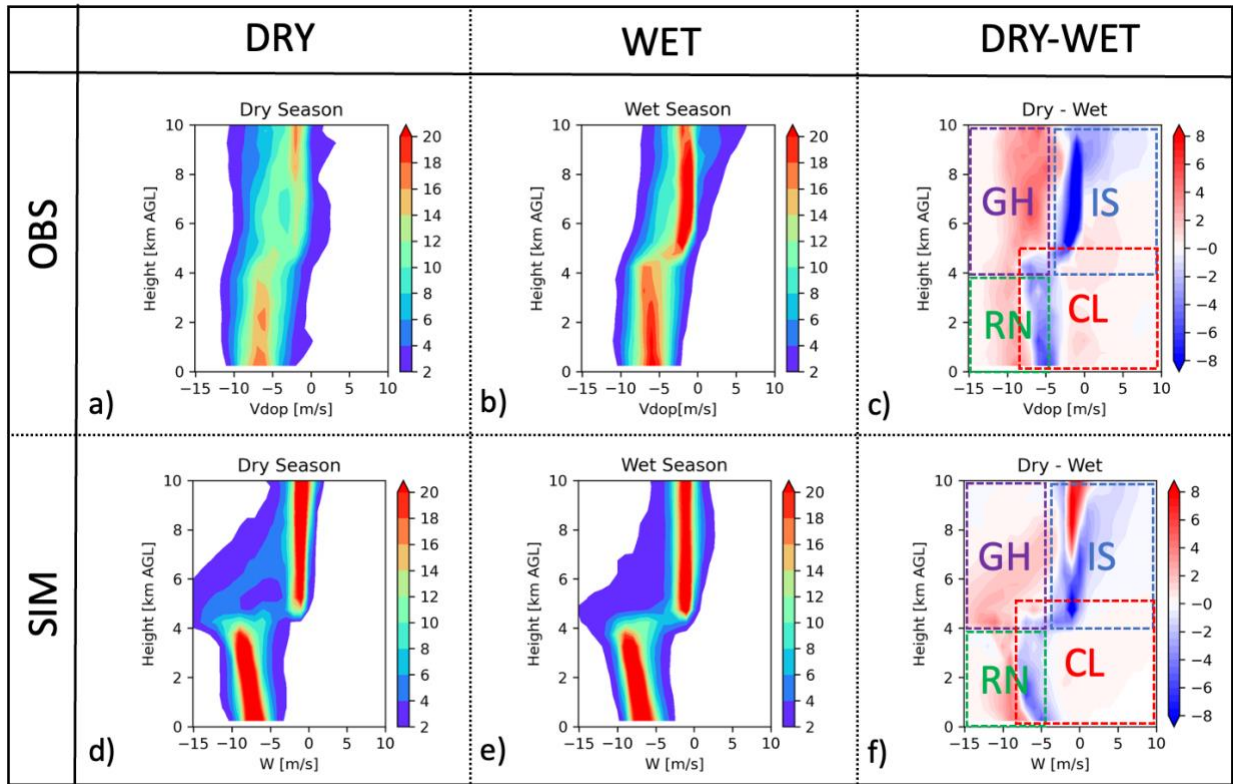
1197

1198

1199

1200





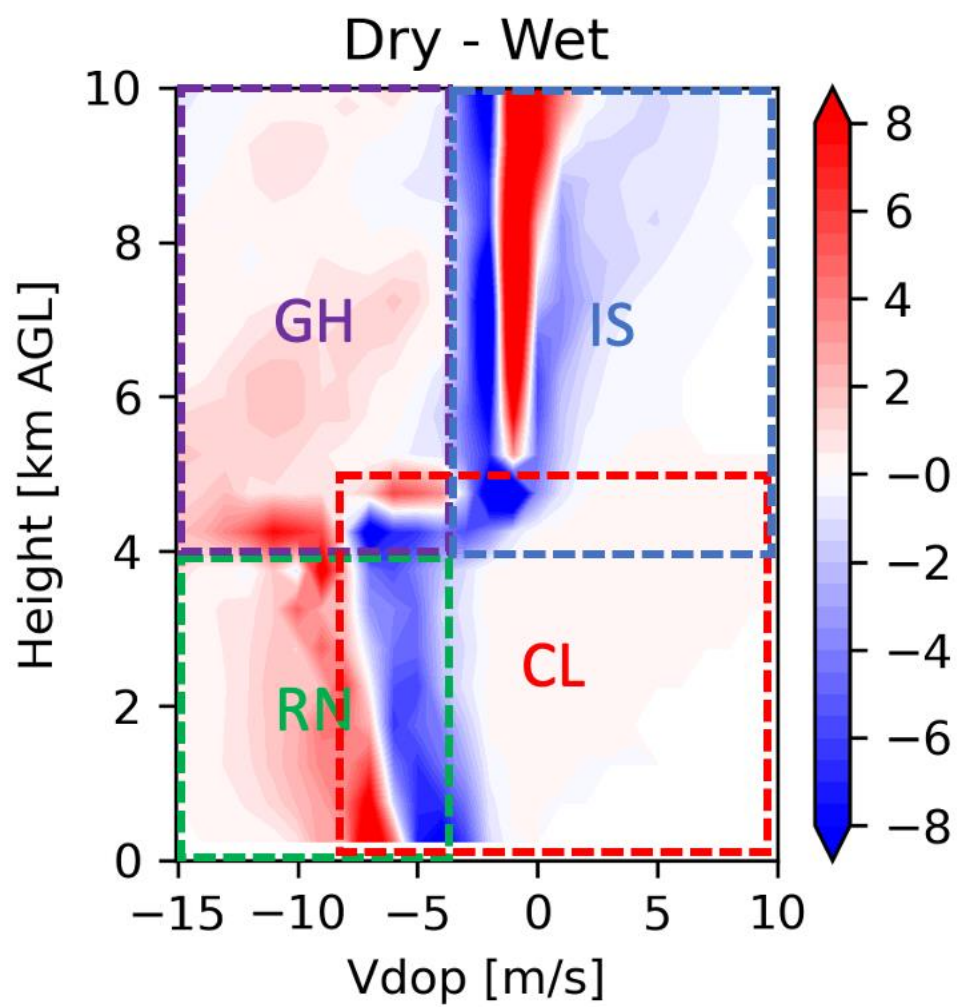
1201

1202 Figure 4. Contoured Frequency of Altitude Diagram (CFADs) of  $V_{dop}$  integrated over dry and wet  
 1203 periods, as well as dry-wet differences. The upper row (a-c) represents observed composites, while  
 1204 the lower row represents simulated composites. CL, RN, IS, and GH represent the hydrometeor  
 1205 regimes defined in Fig. 3.

1206

1207

1208



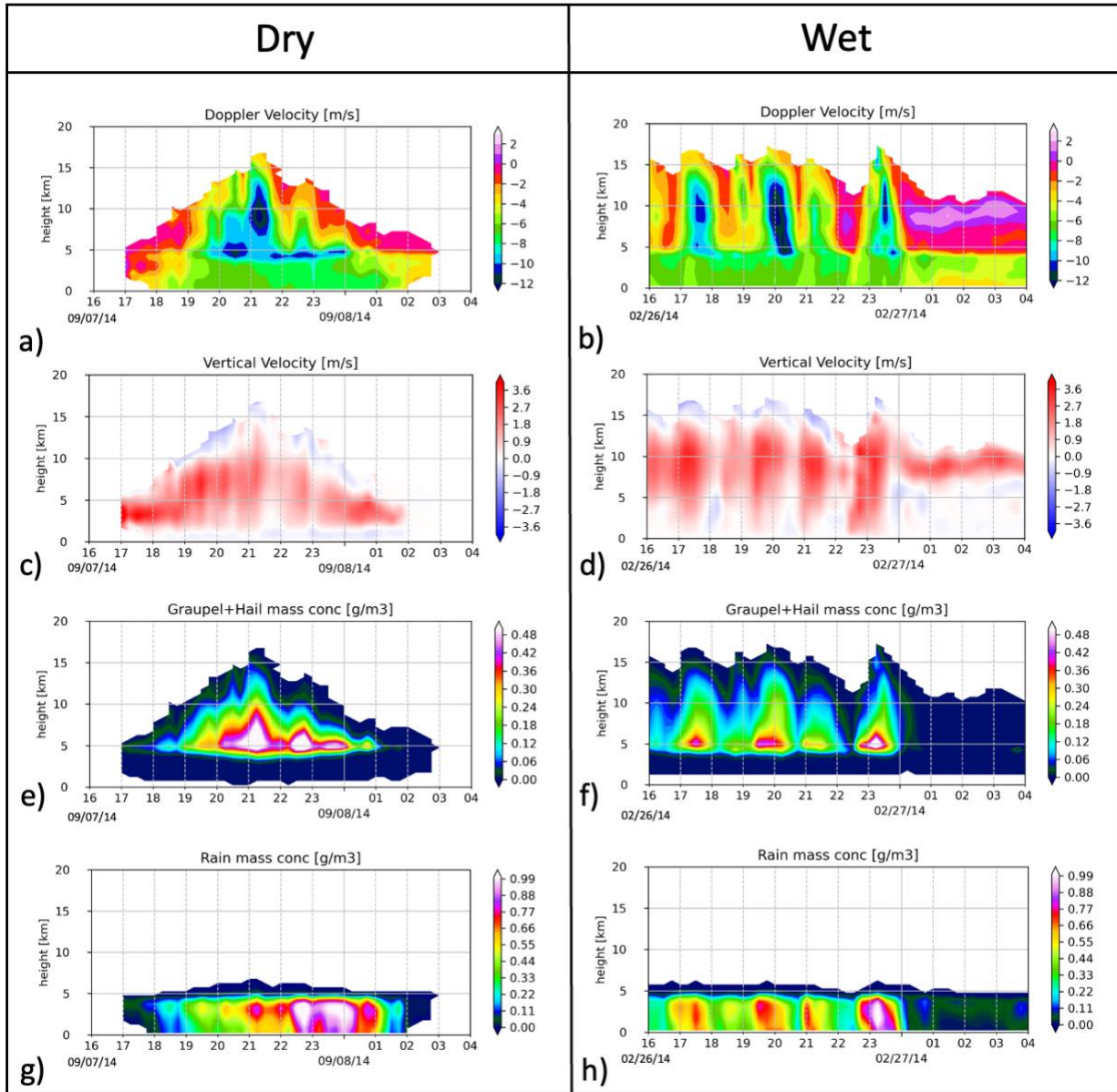
1209

1210 Figure 5. Contoured Frequency of Altitude Diagram (CFADs) of simulated  $V_{dop}$ , differentiated for  
 1211 dry- and wet-season golden cases.

1212

1213



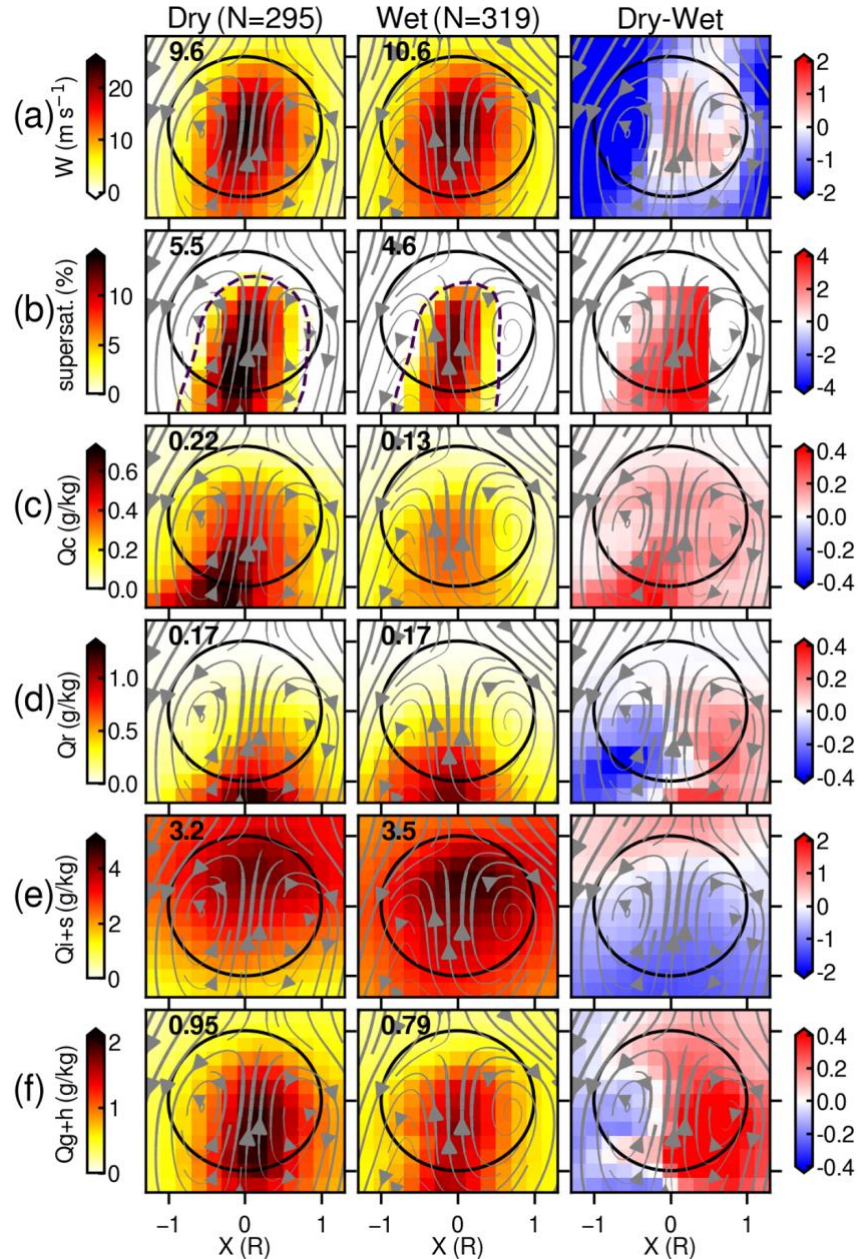


1214

1215 Figure 6. Time series of convective core-mean (a-b) Doppler velocity, (c-d) vertical velocity, (e-  
 1216 f) graupel and hail concentrations, and (g-h) rain concentrations profiles of convective grids from  
 1217 the dry- and wet-season golden cases.

1218

1219

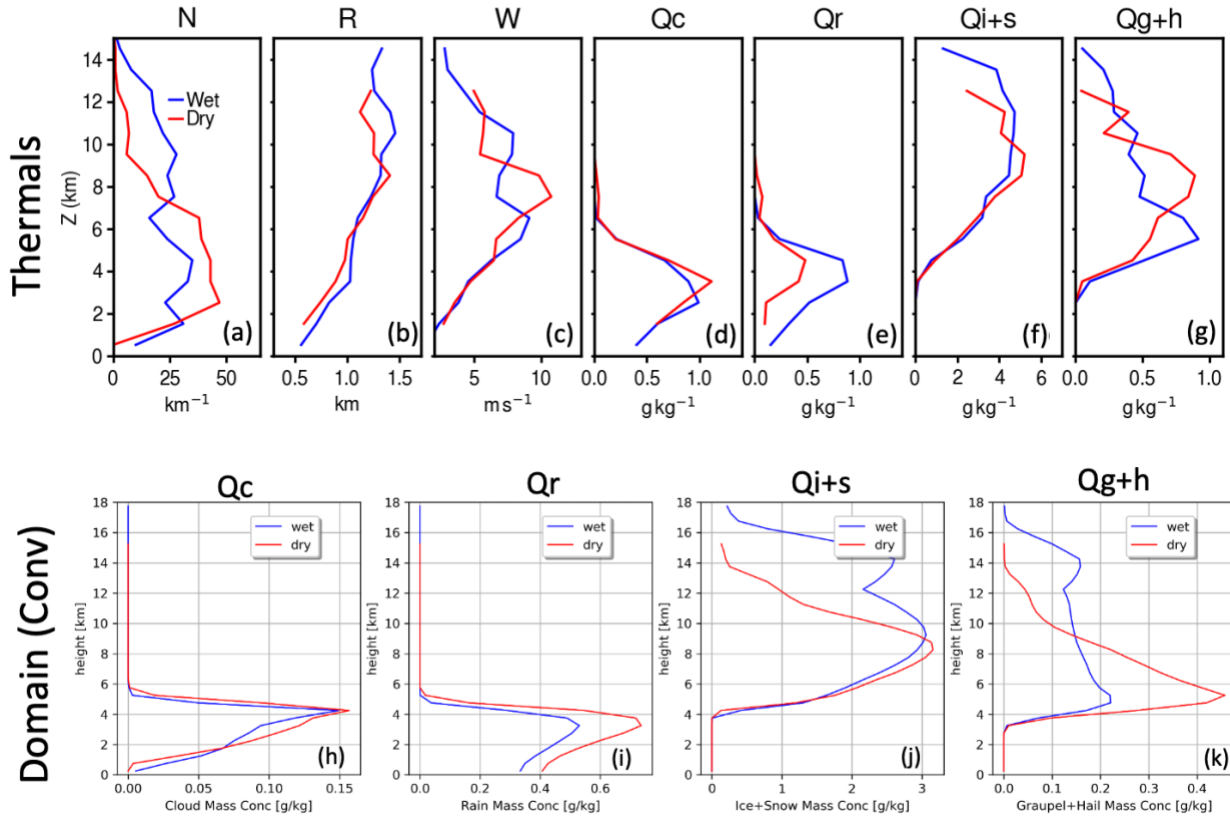


1220

1221 Figure 7. Cross sections along the x-z plane of flux-weighted thermal values of (a) vertical velocity  
 1222 ( $W$ ), (b) supersaturation ( $S$ ), (c) cloud droplet mass concentration ( $Q_c$ ), (d) rain mass concentration  
 1223 ( $Q_r$ ), (e) ice and snow mass concentration ( $Q_{i+s}$ ), and (f) graupel and hail mass concentration  
 1224 ( $Q_{g+h}$ ), for composites of all tracked thermals at the point of their maximum vertical velocity,  
 1225 scaled by their radius (horizontal and vertical coordinates are in units of mean thermal radii). Left,  
 1226 middle, and right column corresponds to the dry-season golden case, the wet-season golden case,  
 1227 and dry-wet case difference, respectively. Upper left values in each panel are the flux- and radius-  
 1228 weighted mean over all samples. Arrows indicate the average flow streamlines in the rising thermal  
 1229 reference frame. The dashed contour in supersaturation values corresponds to 100% relative  
 1230 humidity. These are reference-time ( $t=0$ ) mean values.

1231

1232



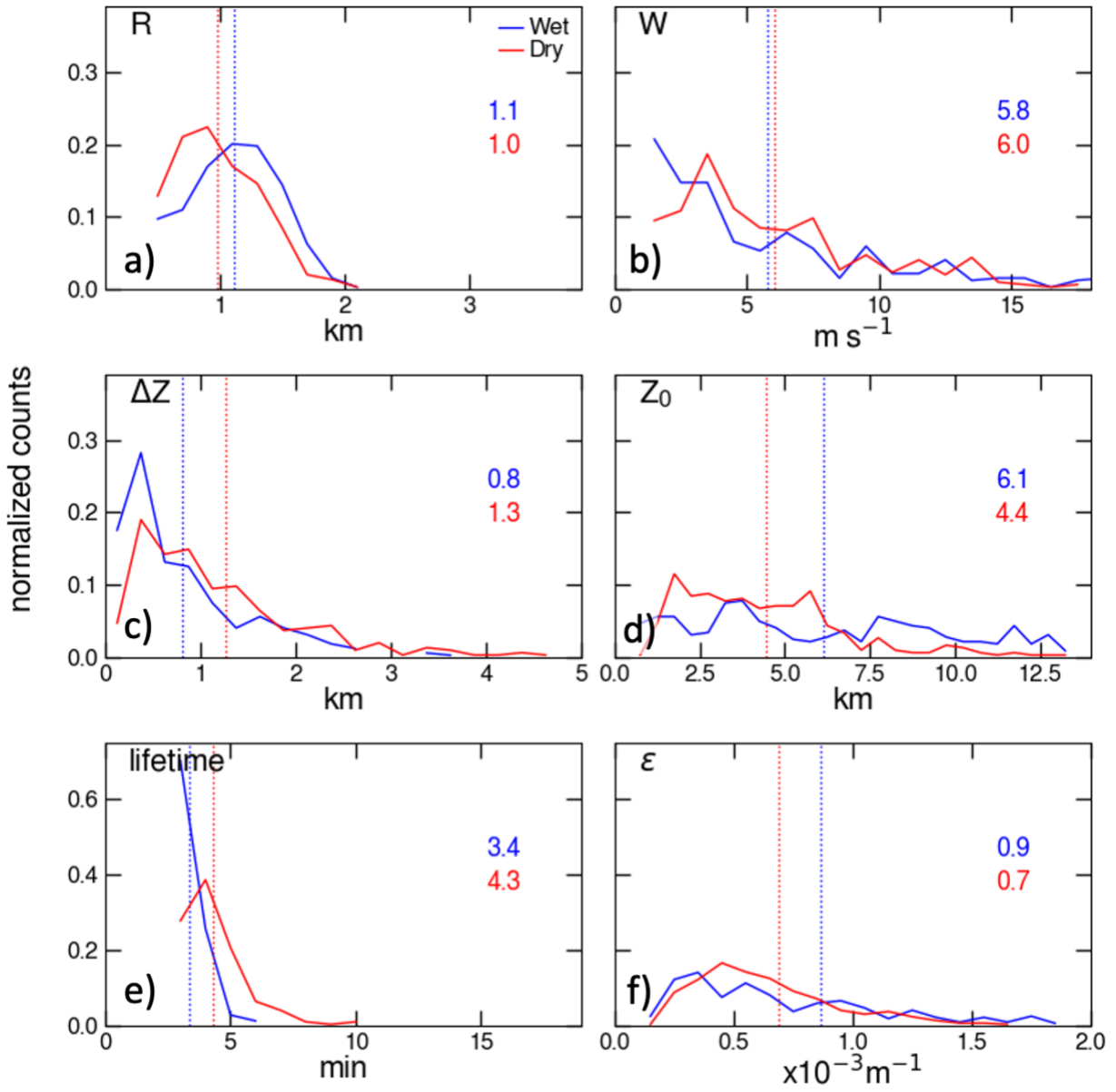
1233

1234 Figure 8. (a-f) Vertical profiles of thermal-mean (a) number concentrations (N), (b) radius (R), (c)  
1235 vertical velocity (W), (d) cloud droplet mass concentration (Qc), (e) rain mass concentration (Qr),  
1236 (f) ice and snow mass concentration (Qi+s), and (g) graupel and hail mass concentration (Qg+h).  
1237 These are all-thermal mean values.

1238 (g-j) Vertical profile of domain-mean (h) cloud droplet mass concentration (Qc), (i) rain mass  
1239 concentration (Qr), (j) ice and snow mass concentration (Qi+s), and (k) graupel and hail mass  
1240 concentration (Qg+h) of convective grids from the dry- and wet-season golden cases.

1241

1242



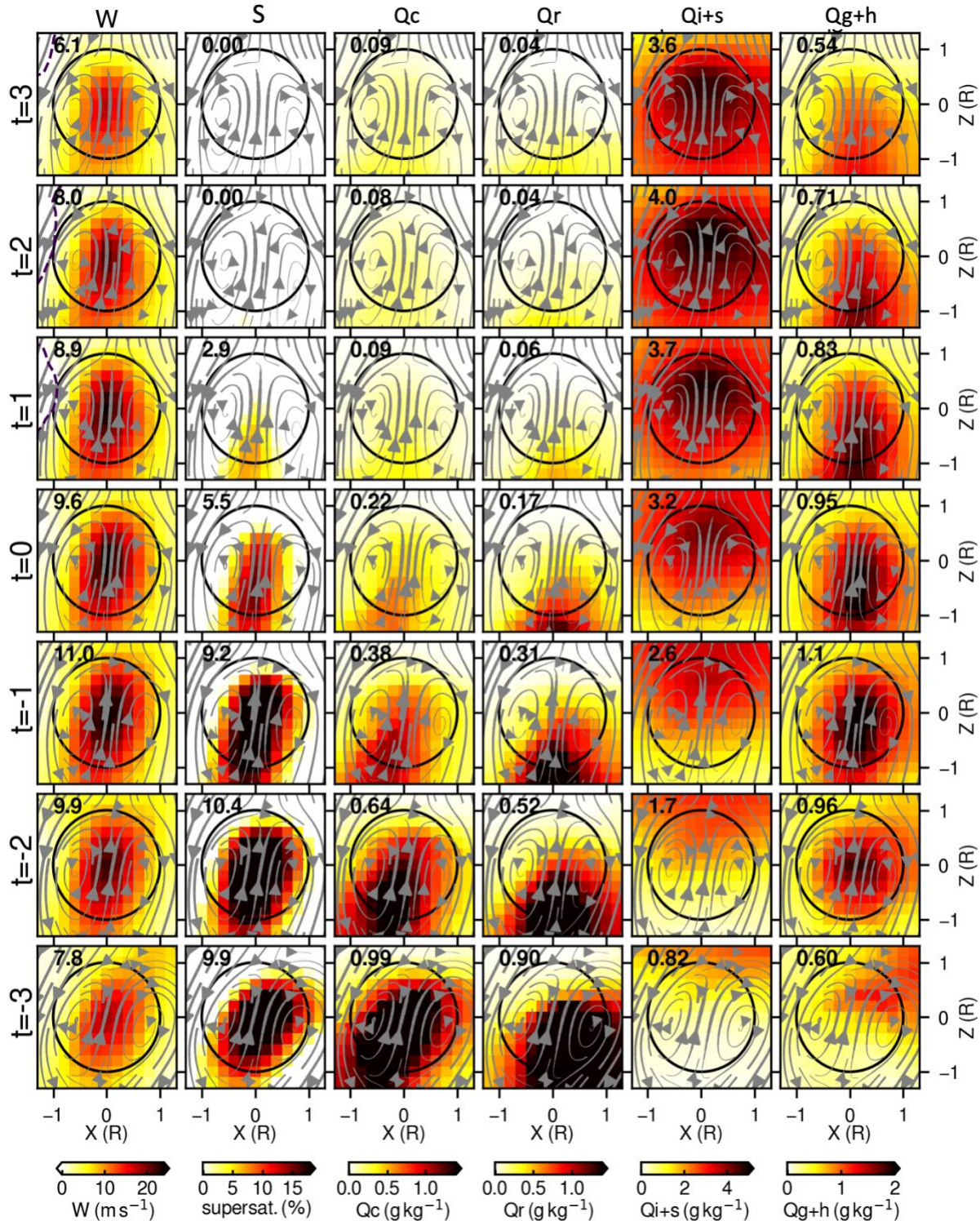
1243

1244 Figure 9. Normalized histogram of thermal (a) radii (R), (b) vertical velocity (W), (c) travel  
 1245 distance ( $\Delta Z$ ), (d) initiated level ( $Z_0$ ), (e) lifetime, and (f) entrainment rate ( $\epsilon$ ) from the dry- and  
 1246 wet-season golden cases.

1247

1248

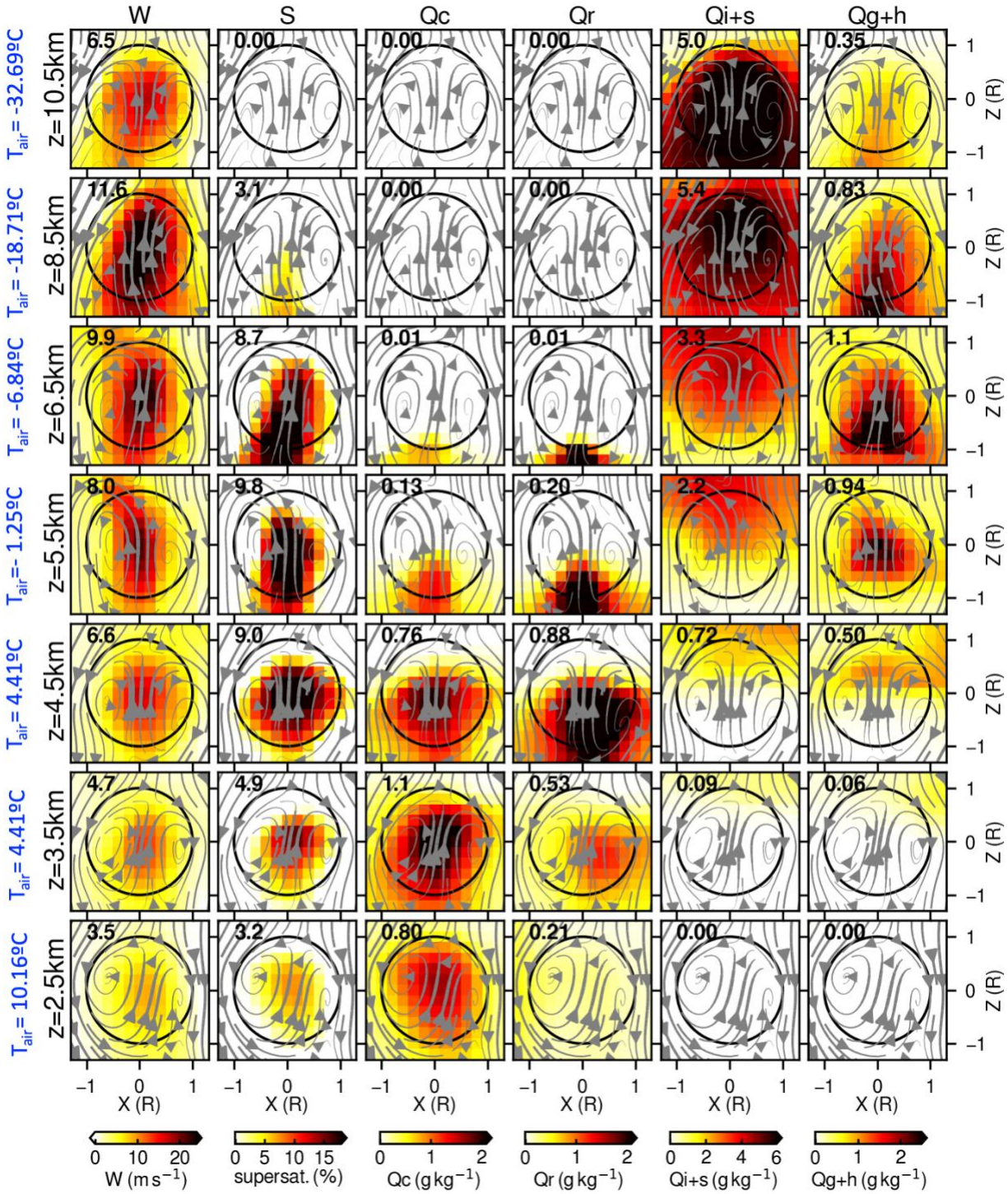




1249

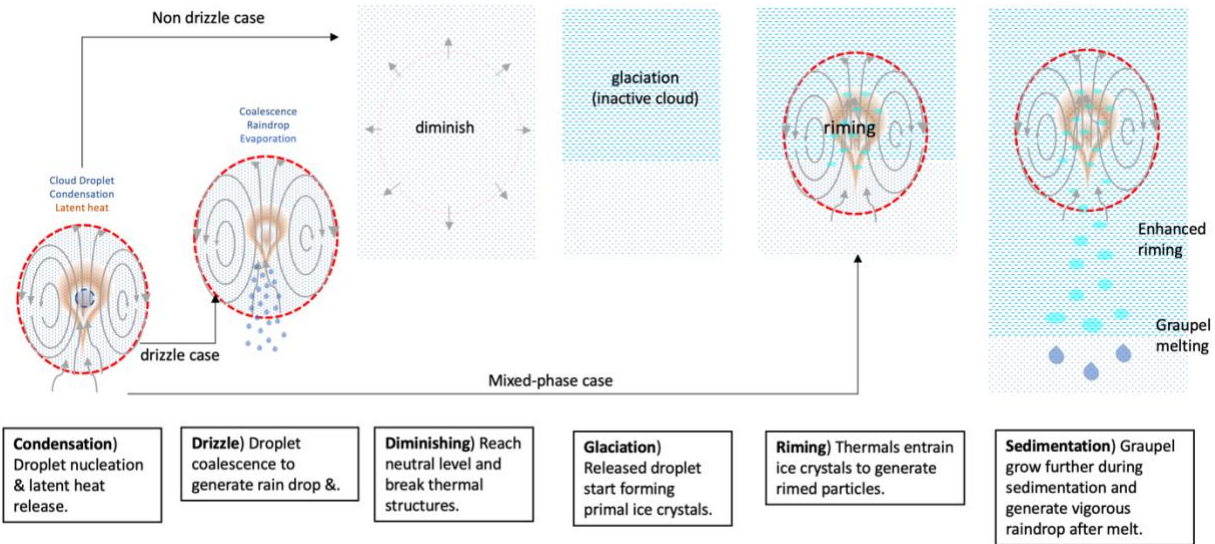
1250 Figure 10. Time series of cross sections along the x-z plane of thermal mean values of vertical  
 1251 velocity, supersaturation values, cloud droplet mass concentration ( $Q_c$ ), rain mass concentration  
 1252 ( $Q_r$ ), (e) ice and snow mass concentration ( $Q_{i+s}$ ), and graupel and hail mass concentration ( $Q_{g+h}$ ),  
 1253 for composites of all tracked thermals scaled by their radius. The time unit is minute.





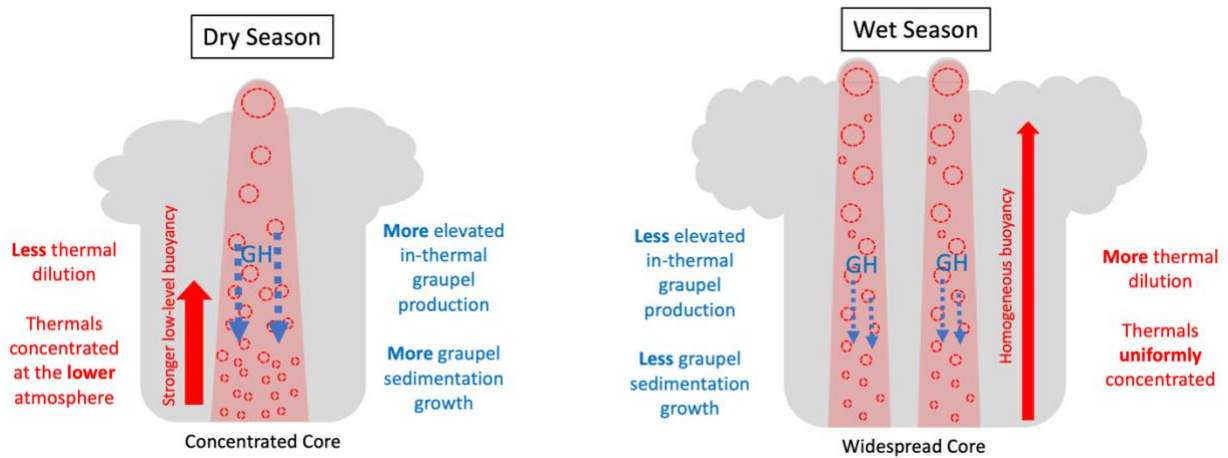
1254  
 1255  
 1256  
 1257

Figure 11. Similar to Fig. 10, but composited at different altitude levels. Note that the shade scales are different from Fig. 10 for clarity.



1258

1259 a)



1260

1261 b)

1262 Figure 12. (a) Diagram of the suggested mechanisms for generating graupel and hail through  
 1263 thermal processes. (b) Diagram of thermal characteristics in deep convection in the dry and wet  
 1264 seasons.

1265